NANOPARTICLE SYNTHESIS AND CHARACTERIZATION: A MECHANISTIC STUDY OF NANOPARTICLE MORPHOLOGICAL EVOLUTION

by

Ross Victor Grieshaber

BS, Chemistry, Gannon University, 2007

BS, Chemical Engineering, University of Pittsburgh, 2008

Submitted to the Graduate Faculty of

Swanson School of Engineering in partial fulfillment

of the requirements for the degree of

Master of Science

University of Pittsburgh

2017

UNIVERSITY OF PITTSBURGH

SWANSON SCHOOL OF ENGINEERING

This thesis was presented

by

Ross Victor Grieshaber

It was defended on

November 16, 2017

and approved by

Robert Enick, PhD, Professor, Department of Chemical and Petroleum Engineering

Robert Parker, PhD, Professor, Department of Chemical and Petroleum Engineering

Thesis Advisor: Judith C. Yang, PhD, Professor, Department of Chemical and Petroleum Engineering

NANOPARTICLE SYNTHESIS AND CHARACTERIZATION:
A MECHANISTIC STUDY OF NANOPARTICLE MORPHOLOGICAL EVOLUTION

Ross Victor Grieshaber, MS

University of Pittsburgh, 2017

The key to designing heterogeneous catalysts for the 21st century is to design them at the nanoscale level with specific morphologies and monodispersity to enhance high product selectivity. This thesis focuses on the synthesis, characterization, and stability of platinum and iron nanoparticles. Control of these nanoparticles monodisperse size and morphology was accomplished through solution phase chemistry. This study has examined two nanoparticle systems to elucidate how of nanoparticle catalysts evolve. The first study focuses on the controlled synthesis of Pt NPs of anisotropic shape and the second study focuses on the carbon encapsulated iron nanoparticle catalysts as they lose morphology.

Platinum nanoparticles have been shown to be quite effective in catalysis technology[1–4]. The structural dependency of the activity and selectivity of the Pt nanoparticles is significant at sizes below 10 nm. Organic surfactants were used to control their size and dispersion in order to ensure that the nanoparticles remain relatively unchanged and stable.

Shape control of Pt nanoparticles was achieved by the addition of Br- ion during the process of polyol reduction of the Pt ions. Changing the ratio of Br- ions to Pt ions yielded a selective growth of nanocubes, cuboctahedra, truncated octahedral, nanoclusters, and polyhedra with a high-

degree of shape monodispersity. These nanoparticles were structurally characterized via transmission electron microscopy to exhibit their local monodispersity of size and morphology.

Iron nanoparticles encapsulated by carbonaceous shells were synthesized by chemical vapor deposition. Transmission electron microscopy (TEM), in situ high resolution scanning electron microscopy, and high resolution transmission electron microscopy (HRTEM SEM/STEM) were used in determine the range of their thermal stability and how the dispersion and morphology of nanoparticles change at elevated temperatures. The carbon encapsulation of the nanoparticles at temperatures below 650 °C. At 650°C, the iron nanoparticles escaped the carbon shells as adatoms and then coalesced in a liquid-like manner. The iron nanoparticles were analyzed in situ and found to undergo particle coalescence and Ostwald digestion at according to nanoparticle diameter, which was attributed to thermal effect and compression of the carbonaceous shell.

TABLE OF CONTENTS

LIST OF TABLES

LIST OF FIGURES

PREFACE

Acknowledgements

I would like to gratefully thank my graduate advisor, Dr. Judith C. Yang, for her support and guidance during my years at the University of Pittsburgh. She allowed me to overcome many obstacles of research and encouraged me to work and think independently.

I would also like to thank my friend and colleague, Dr. Stephen House, for his guidance and assistance in my graduate career. He helped and advised me numerous times with my research and made my time in graduate school a bit easier with his knowledge and friendship.

I would like to acknowledge the Department of Chemical and Petroleum Engineering at University of Pittsburgh, especially my committee, Dr. Robert Enick and Dr. Robert Parker, for their valuable discussions and active participation in helping me during my studies. In particular, I would like to thank, Matthew France, Susheng Tan, Cole Van Ormer and Mike McDonald for their training, analytical services, patience, and their hard work in the Materials Micro-characterization Laboratory (MMCL) and the Nanoscale Fabrication and Characterization Facility (NFCF) at the University of Pittsburgh.

The completion of this thesis would not be possible without help from my friends and colleagues, of whom there are too many to enumerate here. Know that I appreciated my time with everyone I met in and around my graduate studies; you know who you are.

Finally, and most importantly, I would like to thank my parents, Richard and Rosa Grieshaber who always supported and believed in me and told me to follow my heart in all things.

Pittsburgh, Pennsylvania, 2017 **Ross Victor Grieshaber**

1.0 INTRODUCTION

Heterogeneous catalysis is a multi-billion dollar industry per annum[5]. Catalysts can quickly become cost-prohibitive as most have a noble metal, which is a large factor in catalysis as platinum is often more expensive than gold; hence, a key to designing heterogeneous catalysts for the 21st century is to design them at the nanoscale level in order to enhance the surface to volume ratio. These catalysts must be designed with high product selectivity, but not at the cost of activity.

Controlling the nanoparticle morphology, support interactions, and synthetic methods of shape control is key to designing efficient catalyst systems. This study focuses on two nanoparticle systems with applications to heterogeneous catalysis: 1. Synthesis of Pt NPs of anisotropic shape and 2. The synthesis of Fe encapsulated in Fe, their thermal (in) stability and their structural breakdown via migration of iron from encapsulation in carbon at elevated temperatures.

Nanoparticle catalyst systems could provide tailored and improved catalytic properties in comparison to bulk materials. The seminal work of Haruta in 1982, illustrated how gold nanoparticles can behave quite differently from bulk gold and exhibit a high catalytic activity for carbon monoxide oxidation at low temperatures (200K). Boudart differentiated reactions into two groups, those that particle size influenced and those that were not influenced by particle size dispersions. These were heterogeneous metal catalyzed reactions were classified as either "structure-sensitive" or "structure insensitive", respectively in the late 1960s[6]The particle size influences which crystallographic facets are present on the metal surfaces of the particle and therefore the number of unsaturated atoms, as described by Taylor

Somorjai and co-workers have shown that the (100) facets may influence the catalytic activity and selectivity of platinum nanocubes. As the size domain of nanoparticles goes below 10 nm there is a more significant structure dependency on the activity and selectivity of platinum nanoparticles. A smaller nanoparticle of platinum allows for better dispersion of the nanocrystals than larger diameter nanoparticles; this will save on material and ultimately cost. Platinum nanoparticles have been shown to be quite effective in specialized catalysis[1–4], and industrial processes, yet Pt NPs of < 10 nm can be grown by creating stabilize colloids during synthesis

The first part of this thesis deals with the synthesis of anisotropic Pt nanoparticles stabilized by polyvinylpyrrolidone (PVP) and halide ions (Br- and Cl-), in the shape of cubes, cuboctahedrons, truncated octahedrons, dendritic clusters, and polyhedral seeds. Utilizing colloidal synthesis methods for nanoparticle catalysts yielded a narrow nanoparticle size and a higher degree of monodispersity of size and morphology compared to incipient wetness impregnation, galvanic replacement, or ion exchange. Using this technique for the synthesis of Pt nanoparticles we have investigated the growth of anisotropic Pt nanoparticles and investigated the role that the surfactants play in Pt nanoparticle growth.

The second part of this thesis deals with carbon encapsulated iron nanoparticles and their subsequent stability up to ~650 °C where the iron nanoparticles begin to escape from the carbon shells during in situ electron microscopic observation. The previous work of Liu et al. who synthesized SiC nanocones and heterostructures catalyzed by these Fe encapsulated in carbon shells speculated that the Fe diffusion out of the C shell and agglomeration while catalyzing Si C formation is the mechanism for the unusual nanocone structures and Y- and T- junctions. [7,8]. The iron nanoparticles tend escape their encapsulating carbon shells via an Ostwald ripening process.

Iron nanoparticles after escape from the carbon shell, agglomerate, coarsen or shrink depending on the nanoparticle size.

In Chapter 2, the techniques of synthesis and characterization of these materials is described in detail along with characterization equipment such as, transmission electron microscopy (TEM), scanning electron microscopy (SEM) and in-situ TEM heating. The synthesis of anisotropic shape induced Pt nanoparticles is discussed in Chapter 3. The morphological structure of the Pt nanoparticles was examined by transmission electron microscopy. Chapter 4 is focused on the synthesis, growth of the carbon encapsulated iron nanoparticles and their thermal stability and agglomeration. Chapter 5 is a discussion of nanoparticle growth and subsequent deactivation of the Pt and Fe nanoparticle systems mentioned above.

2.0 BACKGROUND

The key advantage utilizing wet chemistry techniques is that they allow for a measure of control over the size and morphology of crystallite grains. Liquid phase fabrication of nanoparticles is sub-divided into three main methods, solvothermal, sol-gel, and synthesis within a structured medium, e.g. microemulsions. These techniques follow a similar three step process, i) reagent solution, ii) liquid-solid nucleation, and iii) a growth stage. Numerous reviews on metal nanoparticle synthesis have been written recently[9–11].

2.1 SYNTHETIC TECHNIQUES

Understanding the control of both nucleation and growth of the nanoparticle is essential to the synthesis of monodisperse nanoparticles of specific morphologies. Nucleation is split between heterogeneous and homogeneous nucleation. The process of nucleation is strongly dependent on decreasing the surface energy, which typically occurs as a heterogeneous nucleation where the activation energy is lowered, i.e. at a phase boundary or impurity site. Homogeneous nucleation occurs when nuclei form spontaneously during supercritical states such as supersaturation. Synthesis of nanoparticles are contingent on both homogenous and heterogeneous nucleation processing occurring concurrently.

Classical nucleation theory was proposed by LaMer and co-workers in the 1950s by the idea of burst nucleation[12]. In the burst nucleation process, nuclei are rapidly formed due to homogeneous nucleation and then grow without any additional nucleation occurring. The driving

idea is that nucleation and growth are separate. The nanoparticle size monodispersity and morphology are subsequently controlled during the growth phase. There are two stages of nanoparticle synthesis namely, nucleation and growth. These stages can be controlled via thermodynamic and/or kinetic considerations as seen in Figure 2.1.

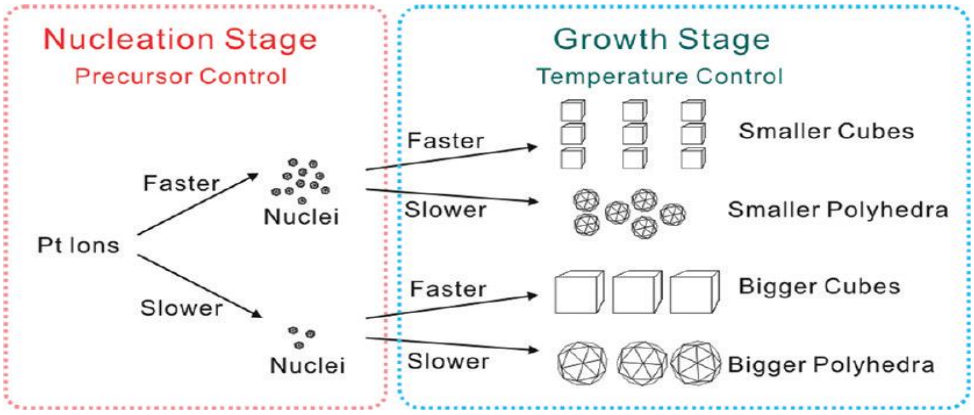

Figure 2.1: Two stage model of nanoparticle nucleation and growth, as described by Tsung et. al. that are mediated by reduction rate kinetics during the two stages[13].

To influence the size and morphology of a nanoparticle system we alter the kinetics of reduction – to change the number of seeds, and the thermodynamics – to change the shapes and final crystallite size. Shape-directed nanoparticles required a two stage seed-mediated growth process to allow these anisotropic features to grow. The following techniques were used to synthesize monodisperse Pt nanoparticles of < 6 nm diameter.

2.1.1 Polyol Synthesis of Noble Metal Nanoparticles

The particular focus of this thesis is particularly focused on the solvothermal synthesis in the presence of micellar ligands to create nanoparticles of well-defined size, shape, and crystallinity. The micelles create nanosized reaction containers, which limit the growth and coalescence of particles. The use of colloidal noble metal nanoparticles date back to the dyes and pigments of ancient historical art of the Romans. The Lycurgus cup is one such piece that dates back to the 4th century. It is famous for being dichroic glass that has minute amounts of gold and silver nanoparticles dispersed in colloidal form through the glass material. Faraday was the first to describe colloids of gold nanoparticles in 1857[14]. Hirai and co-workers prepared colloids of transition metal in polymers by reduction with alcohol in 1979. These metal nanoparticle colloids were stabilized by polyvinyl alcohol, and other primary, and secondary water-soluble alcohols as well as water-soluble ethers. Hirai et al. looked at the protective effect of the polymer ligand, which is attributed to the presence of polar groups from the vinyl polymer[15].

The use of polymer surfactants as stabilizing agents such as polyvinylpyrrolidone (PVP), underpins the foundation of noble metal nanoparticle synthesis in this work. PVP stabilizes the metal nanoparticles by binding to the surface of the nanoparticles and inhibits particle aggregation by steric hindrance. Polyvinylpyrrolidone covalently binds to the metal surface facets through either the carbonyl or tertiary anime of the 2-pyrrolidone (γ-lactam) ring.

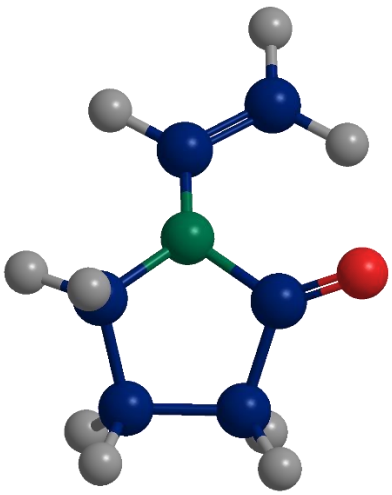

Figure 2.2: Monomer of PVP, the ethyl group is polymerized

In a typical synthesis, the metal salt precursor and surfactant are dissolved (at a ratio of at least 10:1 surfactant to metal salt) in ethylene glycol, water, or ethanol. Once dissolved the reactants are allowed to equilibrate a slightly above room temperature (RT + 5 °C) for a 5 minutes, then the temperature is ramped to reaction temperature for the duration of the experiment (10 min – 20 h). The reaction solution is typically a pale yellow or orange to colorless that undergoes a color change to a deep brown color for platinum nanoparticles.

Surfactant molecules such as PVP are typically composed of a hydrocarbon chain and polar head group that form micelles in colloidal solutions. A micelle is an aggregate of surfactant molecules in a liquid medium which forms when the critical micelle concentration (CMC) of surfactant is obtained. Micelles can only be formed upon addition of further surfactant above CMC and when at or above the critical micellar temperature as known as the Krafft temperature. The thermodynamics of micellar formation is a curious balance of entropy and enthalpy which can be given approximately by Equation 2.2:

$$\Delta G_{micelle} = RT \ln(CMC) \quad (2.1)$$

Micellisation occurs when surfactant molecules aggregate via an entropic effect where the hydrophilic head groups of the surfactant decorate the exterior while the hydrophobic tail groups are sequestered into the center of the micelle formation. A normal phase micelle is referred to as an oil-in-water micelle, whereas an inverse-micelle is referred to as a water-in-oil micelle.

Inverse-micelles created by polyvinylpyrrolidone polymer act as colloidal stabilizing surfactants to enhance metal nanoparticle synthesis *in solvo*[16–27]. The amount of precursor metal salt that is available for particle growth is limited via the micelle volume, which can be tailored by altering the water to surfactant ratio. Polyvinylpyrrolidone (PVP) has been shown to have a dramatic effect on the reactive turn over number (TON) as shown by Baker et al. after removal of the PVP layer. They used UV light to remove most of the PVP from the surface of the nanoparticles to study strong-metal-support interactions (SMSI) via sum frequency generation (SFG) vibration spectroscopy[28]. Krier et al. studied the effect of removal of organic capping layers of colloidal platinum by SFG[29]. Geukens and De Vos studied organic transformations on metal nanoparticles by controlling support-solvent interactions[30]. Amphiphilic polymers are used since they have the ability to coordinate with the particle as well as be solvated in the reaction medium. Electrostatic and steric stabilization are combined in the case of long-chain alkylammonium cations and surfactants, e.g. in reverse micelle synthesis of colloidal metals. There are two methods by which nanoparticles may be stabilized, viz. electrostatic and steric stabilization. Polyol synthesis forms the backbone toward the successful synthesis monodisperse Pt nanoparticles, we used this method it conjunction with facet-specifically bound ions to stabilize the colloidal Pt NPs < 6nm.

2.1.2 Colloidal Stabilization

DLVO Theory of Attraction/Repulsion

At short interparticle distances, two particles are attracted to one another by van de Waals forces which must be countermanded to hinder aggregation. Ionic species have been found to have a profound effect upon reaction mechanism and subsequent growth of nanoparticles. Historically, Faraday used phosphate ions to reduce his gold precursors into a colloid of gold nanoparticles. For instance, during the reduction of chloroauric acid in aqueous solution by sodium citrate, the gold nanoparticles are surrounded by an electrical double layer of adsorptive citrate, chloride ions, and cations that are attracted to the particles[31]. This creates a coulombic repulsion between the particles; the attractions of inter-particle van der Waals forces are much weaker than electrostatic forces between adsorbed ions and counter-ions. If the electric potential within the electric double layer (EDL) is sufficiently high, the ions will repulse one another creating a stable suspension[17,24,32–36]. In DLVO theory, the basic assumption is that the total force between colloidal particles in the addition of the van der Waals (attractive) and the EDL (repulsive) forces[37]. Displacement of adsorbates, e.g. neutral species, temperature and subsequent thermal motion can disrupt the ions allowing for agglomeration of particles. In this study, the Br- ions and positive counter ions arrange in an EDL around the Pt nanoparticles.

2.1.3 Facet-specific Capping Agents

There are numerous capping agents such as the anions of the metal precursor, solvents, surfactants, polymers, gas molecules, etc. Halide ions (Br^-, I^-, Cl^-) are typically used to cap (100) facets for a majority of face-centered cubic (FCC) metals[38,39]. Bromide and iodide ions present a stronger

facet-selectivity for cubic growth compared to chloride ions[17]. Numerous capping agents bind to specific facets, lowering the surface energy of the nanocrystals. Organic solvent systems allow amines and acids as capping agents, however their exact mechanistic role as facet promoters is not clearly understood at present. Alkyl groups affect the interaction between these species and different metal facets.

It has been demonstrated for platinum based alloys that when the length of the alkyl group was increased that the exposure of the (100) facets would be favored[40]. Oleic acid was shown to bind weakly to platinum and facilitates the growth of cubes, but also favors the aggregation of the nanoparticles[41]. Benzoic acid can be as a {111} facet-specific binding agent, which inhibits the growth on (111) facets of Pt-Ni alloy as shown by Li et al.[42]. Citric acid has been shown to be a {111} facet specific capping agent in platinum and palladium NCs[43].

Carbon monoxide in the presence of oleylamine was shown to stabilize the {100} facets of Pt and the {111} facets of Pt_3Ni alloy[44].The effect of CO is altered as the solvent composition changes. CO in conjunction with oleylamine was used to stabilize {100} facets on nanocubes; however, if the CO/oleylamine was used in the presence of biphenyl ether then nanooctahedrons exposing {111} facets were formed[45]. Dimethylformamide is a common solvent in solvothermal syntheses, which displays facet-specific capping abilities as shown by Carpenter et al. in their Pt-Ni alloy NCs[46]. The ratio of Pt:Ni determined whether the NCs tended to expose {100} facets via a cubic morphology or {111} facets via an octahedral morphology if the ratio was high or low, respectively.

In the oxidative etching process, halide ions assist dissolution of O_2 to dissolve the surface atoms[47]. Halide ions such as Br^- ions in particular, strongly bind onto (100) facets; the concentration of halide ions around (100) facets is significantly higher than that around the other

facets. Citrate ions are able to competitively adhere to the surface of the nanocrystal, which can be used to retard or hinder the oxidative etching process[48]. Based on the success of Br- ions to bind the (100) facets, we investigated the growth of Pt nanoparticles into anisotropic shapes.

2.1.4 Encapsulated Core-Shell Nanoparticles

The core-shell architecture is one of the most studied metallic nanoparticle catalyst systems. Synthesis of core-shell nanoparticles (NPs) of expensive noble metals has been done previously; however, there has been renewed interested in utilizing inexpensive first-row transition metals (Fe, Co, Ni, etc.). Transition metals with a core-shell morphology have revealed novel physical properties which approach those of noble metals[49]; these nanoparticles can be an alternative to expensive noble metal materials. Core-shell NPs allow for a diverse applications by combining properties of different materials, such as target drug delivery in controlled release, environmental protection of the core material from poisoning, as well as enhancing magnetic resonance imaging in vivo[50,51].

2.2 ELECTRON MICROSCOPY TECHNIQUES

2.2.1 Transmission Electron Microscopy

Transmission electron microscopy (TEM) is a powerful and versatile tool for providing morphological, size (and distribution), and chemical information of individual nanoparticles with sub-unit-cell spatial resolutions, essential for determining structure-function relationships.

A typical transmission electron microscope is composed of: an illumination system, a specimen stage, an objective lens system, the magnification system, the data recording system(s) and, the chemical analysis system[52] as seen in Figure 2.3. The electron gun typically employs either a thermionic emission source (e.g. LaB_6 or tungsten filament) or a field-emission source. The illumination system is also comprised of condenser lenses that are vital to forming a fine probe. The specimen stage can be used to observe a myriad of phenomena resulting from processes such as mechanical stress, magnetic stress, an electric field, or thermal annealing. Beam-sample interaction is also a possible event that may or may not be intended during specimen characterization. The objective lenses are what determine the image resolution limit. The magnification system is comprised of intermediate lenses and projection lenses, which may yield a magnification up to 1.5 million. The data recording system is usually a digital system combined with a charge coupled device (CCD) camera that allows for data processing and quantification. The chemical analysis system is typically the energy dispersive X-ray spectroscopy (EDS) and electron energy-loss spectroscopy (EELS); these techniques can be used in concert to complement one another to quantify the chemical composition of the specimen.

A B

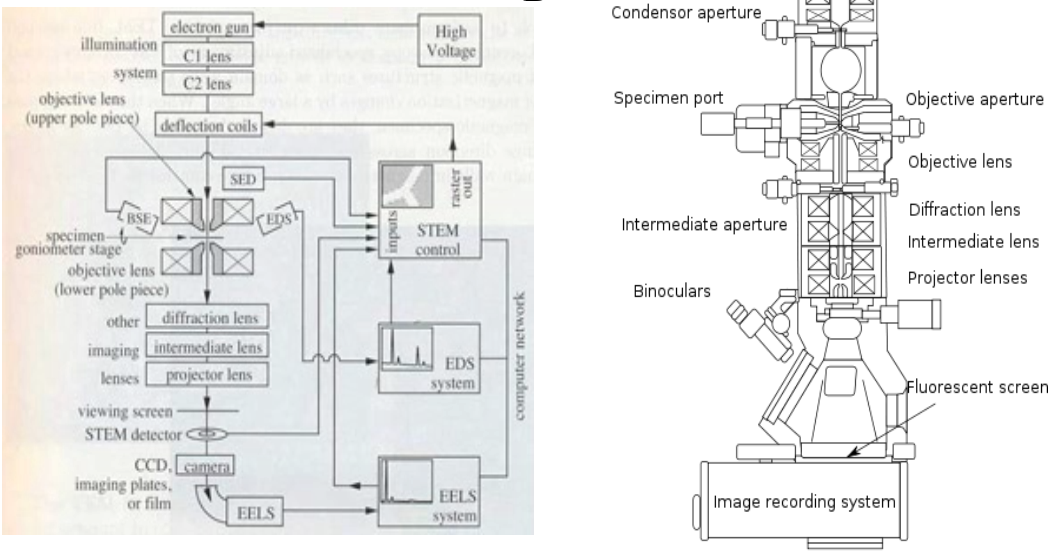

Figure 2.3: (A) Schematic Diagram of Transmission Electron Microscope and Detectors, (B) Representation of Transmission Electron Microscope Column Setup[52]

Image formation in transmission electron microscopy is analogous to optical microscopy in that both have an illumination source and lenses where appropriate. However, the resolution of an optical microscope is limited by the wavelength of light. Louis de Broglie showed that particles of matter propagate as waves, from this the wavelength of propagating electrons at a given accelerating voltage can be determined by:

$$\lambda = \frac{h}{\sqrt{2meV}} \tag{2.2}$$

When imaging in a TEM, images are formed by either using the central spot, or by using a portion or the entirety of the scattered electrons. Most of the scattered or diffracted electrons are

blocked from the imaging plane detectors by a small objective aperture. This aperture determines which electrons reach the detector for image contrast. The method by which we choose electrons determines whether the images will be bright field (BF) or dark field (DF) images; imaging with the direct transmitted beam produces bright field images, whereas the scattered electrons will form dark field images. The magnification of images is adjusted via the intermediate lenses of the microscope. Image contrast is formed by amplitude, phase, mass-thickness, and Z contrast. A JEOL JEM 2100F, 200keV LaB6 instrument with resolution of 2 A, was utilized to characterize the shapes and monodispersity of the Pt nanoparticles as well as the Fe encapsulated in carbon.

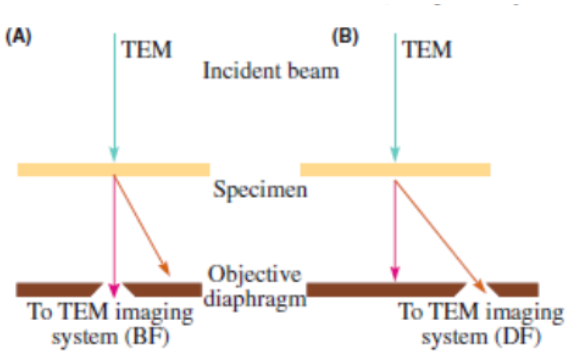

Figure 2.4: Adapted from Williams and Carter, a comparison of the use of an objective aperture in TEM to select (A) the direct or (B) the scattered electrons forming BF and DF images, respectively[53].

High resolution microscopy allows for the particle shape morphology, crystal lattice structure(s) and grain boundaries to be clearly determined. Facets of nanoparticles are often well-defined in HRTEM images. The technique of high resolution transmission electron microscopy (HRTEM) uses a larger objective aperture (in comparison to BF or DF imaging). The transmitted

beam can interfere with a multitude of diffracted beam and create contrast due to the relative phase of the beams. High-resolution TEM uses phase contrast to form images of atomic columns of crystalline materials, typically of material thicknesses less than 10 nm.

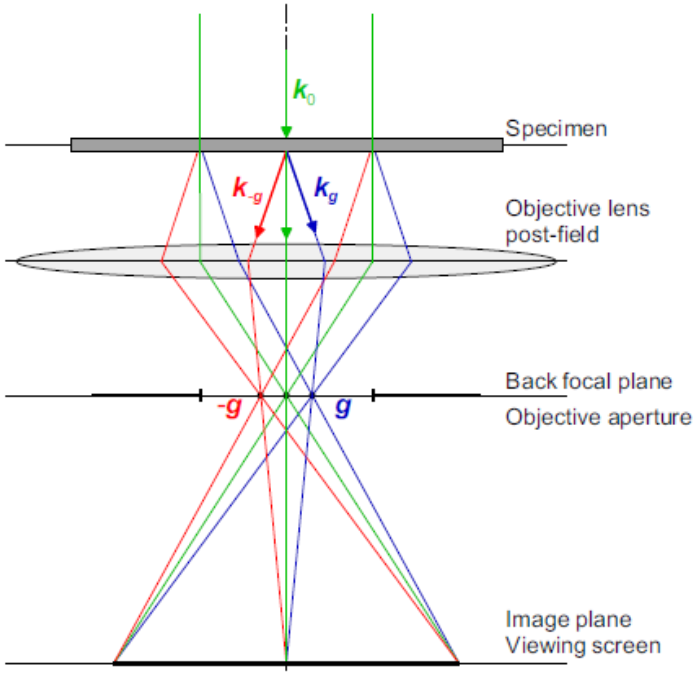

Figure 2.5: HRTEM imaging. Transfer of the exit-plane wave by the post-field of the objective lens to the viewing screen[54].

High-resolution images are primarily affected by focus and specimen thickness, however other factors such as acceleration voltage and mechanical stability, high-gun brightness, and spherical aberration constant (C_s) affect HRTEM image quality. HRTEM was used to characterize platinum nanocrystal size, dispersion, and morphology as well as the Fe nanoparticles encapsulated in carbon.

A JEOL JEM 2100F FEG microscope operating at 200kV was used to collect the images of platinum nanocrystals at the Nanofabrication and Characterization Facility at the University of Pittsburgh. This JEOL JEM 2100F is equipped with attachments for XEDS analysis and a GIF-TRIDIEM post-column energy filter for acquisition of energy-filtered images and diffraction patterns. The instrument utilizes a Schottky field-emission gun (FEG) at 120 kV up to 200 kV, which achieves a 2.2 angstrom point resolution and an information limit of 1.6 angstroms. In TEM and STEM mode, the field-emission gun yields intense electron point probes with diameters from 5 angstroms and 1.6 angstroms, respectively; allowing sufficient current for localized diffraction as well as compositional and chemical analysis with sub-nanometer resolution in phase contrast imaging.

The Hitachi High Technologies H-9500 is another HREM instrument available at the Nanoscale Fabrication and Characterization Facility (NFCF). This is an environmental electron microscope that is specifically designed for in-situ observations at environmental conditions up to 10^{-2} Pa. The instrument utilizes a lanthanum hexaboride (LaB_6) electron source that ranges from 100 kV up to 300 kV, which achieves a 1.0 angstrom lattice resolution and a 1.8 angstrom point-to-point resolution.

Available for use for this instrument is a single-tilt and double-tilt specimen holders, as well as an Aduro™ heating holder from Protochips that can heating a specimen from room temperature up to 1000°C at a heating rate of 10^6 °C/s. with/out a gas, e.g. H_2, O_2, CO, CH_3OH, or CH_4. This heating holder was used in the Hitachi H-9500 to visualize the changes to the Fe encapsulated in C at the angstrom level at elevated temperatures. It is also equipped with Bruker Quantax energy dispersive spectroscopy (EDS) system for elemental analysis at TEM mode.

2.2.2 Scanning Electron Microscopy

A scanning electron microscope (SEM) also utilizes electrons for imaging however the image is of the surface of the sample. The accelerating voltage of an SEM is typically ~20 keV or less, where backscattered (1 – 20 keV) or secondary electrons (ca ~0.01 – 0.5 keV) are detected. The electron beam is swept across the sample in a raster pattern to detect how the electrons are interacting with the sample. The interaction between the electron beam and the sample is coulombic.

There are two main type of scattered radiation, elastic and inelastic. Elastic scattering is represented mostly by coherent scattering with no loss of energy. Inelastic scattering is represented by scattered electrons that have less energy than the incident beam. Backscattered electrons are generated from elastic scattering of the coherent incident electron beam and the sample. Secondary electrons are generated from inelastic scattering interactions between the coherent incident electron beam and the sample. Both SE and BSE are from the surface of the sample with a penetration depth of ~1 nm and 10-100 nm, respectively. The utilization of SE imaging allow characterization of surface morphologies.

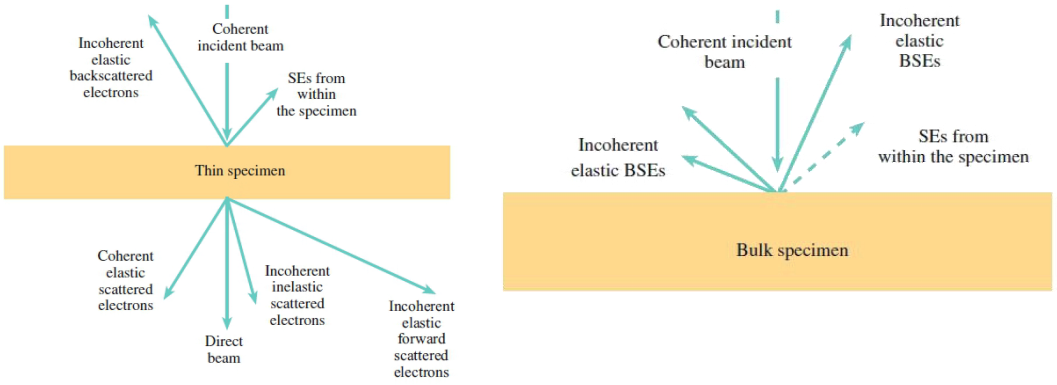

Figure 2.6: Electron beam interaction with thin sample (left) and bulk sample (right) and electron scattering events of interest[53].

The significant advantage of scanning electron microscopy is that thick samples that cannot be transmitted through can still be imaged, however the resolution is quite low compared to transmission electron microscopy.

The Hitachi High Technologies S-5500 field emission scanning electron microscopy/scanning transmission electron microscope (FE SEM/STEM) at maximum magnification of 2,000,000 and a secondary electron point resolution of 0.4 nm at 30 kV, nanoparticles 5–10 nm can be imaged. A Hitachi S-5500 SEM/STEM microscope was used to collect data of carbon encapsulated nanocrystals at the RJ Lee Group, Inc. located in Monroeville, PA 15146, USA. The S-5500 is a unique instrument that has the ability to simultaneously, which provided critical insight on the agglomeration of the FE NPs. collect secondary electron images (SEIs), bright field or dark field STEM images without having to change the position, and is

equipped with an energy dispersive x-ray spectroscopy (EDS) system. The SEM/STEM gives the ability to image the surface and interior simultaneously. A Protochips heating holder (Aduro^{TM}) was used to heat the carbon-encapsulated Fe nanoparticles.

3.0 PLATINUM NANOPARTICLES

3.1 INTRODUCTION

Synthesizing nanoparticles with a particular morphology is paramount to increasing catalytic efficiency as chemical reactions are more easily catalyzed by a particular facet(s) over another. For example, the (100) facets of Pt are active for oxygen reduction and hydrogen containing reactions, while oxidation of primary alcohols and carbon monoxide are in the domain of the (111) facets. Nanocubes enclosed by (100) facets are more active for certain reactions by many times[55]. Thus, it is important to synthesize monodisperse, well-formed structures and to characterize their structure[35,56–62]. In this work, Pt nanoparticle morphologies consisting of cubes, truncated octahedrons, cuboctahedrons, nanoclusters, and polyhedrons were grown. These morphologies have different percentages of low-index facets which dominate their surface(s). In particular, the cubic morphology consists almost entirely of (100) facets, which comprise the cubic surface. The truncated octahedron has a mixture of (100) and (111) facets. The cuboctahedrons are bounded with (111) facets primarily.

The morphology of nanocrystal shapes are sensitive to preparation conditions, such as temperature and surfactant species used to stabilize the particles. Platinum nanocrystals were grown via inverse micellar encapsulation by a surfactant such as polyvinylpyrrolidone (PVP) or ionic surfactants such as cetyltrimethylammonium bromide (CTAB). The platinum metal salts were reduced in a one-pot polyol synthesis method. The use of ethylene glycol as the solvent in the polyol synthesis process is two-fold: first as the solvent medium and second as a mild reducing agent. Reduction rates were principally altered by changing temperature, reaction time, and species

of reductant (e.g. sodium borohydride, $NaBH_4$). Specific shape morphologies were induced by introduction of directing-agents such as halide ions (Br^-) which bind to preferentially facet-specific sites[63–65], i.e. (100) facet planes, blocking growth on those particular family of facet planes. Therefore, the other low-index facets, (110) and (111) are able to grow unhindered creating anisotropic nanoparticles of e.g. cubic, octahedral, and truncated octahedral.

3.2 EXPERIMENTAL

3.2.1 Synthesis of Platinum Nanocubes

Pt nanoparticles were synthesized from adapted literature methods[66,67,68]. A seed-mediate growth according to the polyol reduction method was used in conjunction with ionic colloidal stabilization to growth anisotropic platinum nanoparticles. In a two-step synthesis consisting of ammonium hexachloroplatinate and ammonium tetrachloroplatinate (Pt^{+4} and Pt^{+2}) reduction. Ethylene glycol acts as a solvent as well as a reducer in this reaction to reduce the metal salts to metal nanoparticles. Polyvinylpyrrolidone (PVP) was used to created micelles that act as templates to synthesize NPs of monodisperse size and morphology by polyol reduction. Pt nanocubes were grown by limiting the size and morphology by polyvinylpyrrolidone (PVP) micelle synthesis and direct the shape growth by Br ion addition. Anisotropic growth is initiated by the facet-capping effect of the PVP; the capped sites allow for the (100) facets to become dominant.

The solution is allowed to equilibrate for an hour, and is then heated to a temperature of 175 ˚C in an oil bath. The solution was maintained at this temperature for 20 minutes, with refluxing conditions and magnetic stirring. A colorimetric change will evolve as the reaction

occurs, resulting in a dark brown solution. Once cooled, the solution is washed of the excess polyvinylpyrrolidone (PVP) by using 100 ml of acetone during the subsequent washing cycles. The suspension needs to then be centrifuged at ~3000rpm for ~10 minutes. Upon centrifugation, the colorless supernatant is discarded and then the black solid product was dispersed in ethanol and then precipitated by hexanes three times (20:80 ml). The nanoparticles can be re-dispersed in ethanol (10 ml) to be transferred to ultra-thin carbon/Cu grids for TEM characterization.

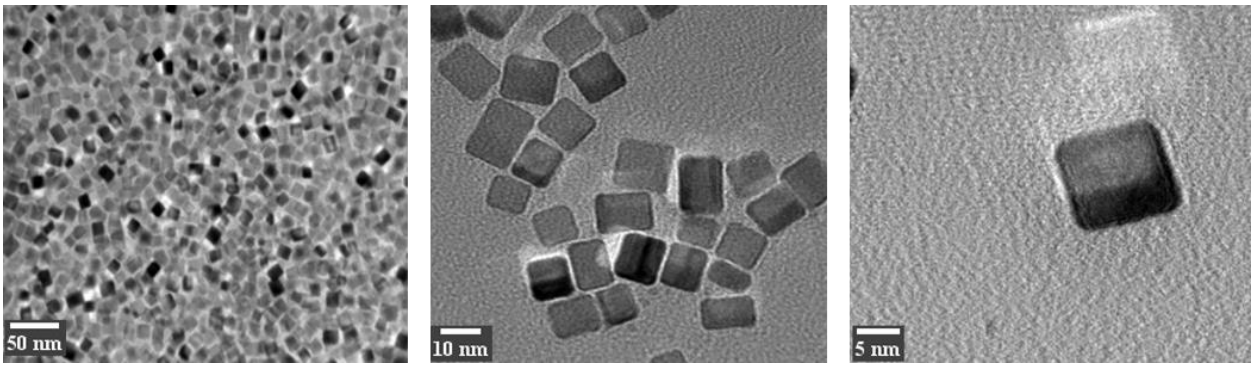

Figure 3.1: Pt NPs nanocubes of 5.1±2.3 nm were grown from the seed-mediated growth and 7.3±1.8 nm for the bromide mediated synthesis.

In a typical synthesis, 57.0 mg of H_2PtCl_4 was dissolved into 3.0 ml of deionized water, and mixed by vortexing or shaking for 1.0 h. Do not mix the sample by sonication as this will begin the process of reduction of the metal precursor. To another vial add 105 mg PVP, 250 mg KBr, and 60 mg ascorbic acid then proceed to mix into 8.0 ml of deionized water and allow the chemicals time to dissolve as necessary (vortex or sonicated). The reducing surfactant mixture (PVP, KBr, and ascorbic acid mixed solution) was then added to the first reaction vial. Replace

the cap and wait ~5 minutes until the temperature has reached 75 °C with temperature controller. After the surfactant mixture has equilibrated, add 3.0 ml of the H_2PtCl_4 solution to the reaction vial quickly via injection port. The reaction will take approximately 3.0 h and the vial should be naturally cooled down after the reaction. Transfer the reaction solution to 1.5 ml centrifuge tube and then spin down the product at 13,000 rpm for 10-20 minutes. The nanoparticles can also be separated by mixing the reaction solution with ~25.0 ml acetone, transfer the solution to 1.5 ml or 50 ml centrifuge tube and then spin down the product @ 10,000 rpm for 10-20 minutes. Size fractionate nanoparticles via centrifugation, re-dispersion/sonication cycles as necessary. Pt nanoparticles are ready to be characterized by re-dispersing in ethanol to be transferred to ultra-thin carbon/Cu grids for TEM characterization.

Platinum nanoparticles in an aqueous solution phase were stabilized by polyvinylpyrrolidone (PVP) and reduced slowly by ascorbic acid. Potassium bromide was introduced to help facilitate a cubic shape; the Br- ions tend to adhere to the (100) facets of the platinum nanoparticles which inhibits restricts growth, allowing the cubic shape to evolve as the particle increases in size from seed to final shape. The particle sizes were measured by transmission electron microscopy to be nanoparticles nanopolyhedra seeds of ~2.6 nm and 5.1±2.3 nm nanocubes for the seed-mediated growth and 7.3±1.8 nanocubes for the bromide mediated nanoparticles.

3.2.2 Synthesis of Cuboctahedrons

In an aqueous phase solution of deionized water, K_2PtCl_4 metal salt was prepared and stabilized by myristyltrimethylammonium bromide (TTAB). In a typical synthesis, add 10.0 ml of H_2O to a 3-necked flask (allow a needle to vent gas through a septum). Dissolve in 100.0 mM

TTAB, 2.0 mM of K_2PtCl_4, and allow solution to equilibrate for ~5 minutes at 70 °C. Inject 10.0 mM of ice-cold $NaBH_4$ through the septum and wait for ~20 mins. Centrifuge and wash (with hexane and ethanol cycle) at least three times. Pt nanoparticles are ready to be characterized by re-dispersing in ethanol to be transferred to ultra-thin carbon/Cu grids for TEM characterization.

The solution is aged overnight to allow the solution to equilibrate. The metal salt solution is reduced via cold sodium borohydride ($NaBH_4$) in aqueous solution which is a strong reducing agent which forms $NaBOH_2$ and H_2 in water. A slower reduction step with less reducing agent allows for particles to create less seeds. Slower reducing agents yield larger particles as there are fewer nuclei to grow around, which allows for more growth ripening of particles in the tens of nanometers. An excess of surfactant is used to ensure micelle formation; the amount of surfactant will play a part in determining the size of the final particle ensemble. Over the course of a few hours a colorimetric change occurs resulting in the yellowish-orange solution becoming increasingly brown as more and more reduction and formation occurs. Upon subsequent washing and centrifugation steps, the particles are ready to be transferred to TEM grids for characterization by transmission electron microscopy to determine particle morphology[67].

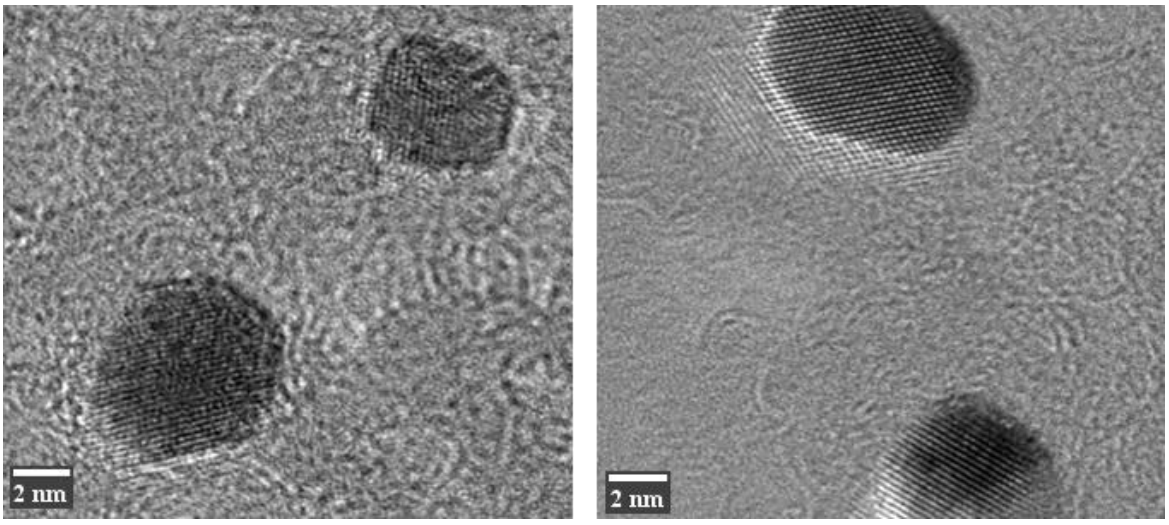

Figure 3.2: The cuboctahedral shapes are dominated by (111) facets which have been shown to promote the production of cyclohexane selectively[67].

3.2.3 Truncated Octahedral Nanocrystals

In an aqueous solution of deionized water, PVP (MW=~55,000), L-ascorbic acid and citric acid were mixed together. The two acids have different reduction kinetics which allows the nuclei to form and then in turn become seeds via the autocatalytic growth process. Further addition of surfactant and metal salt into the solution will yield a branched structure of dendrites formed upon the surface of the seeds from the initial solution[69].

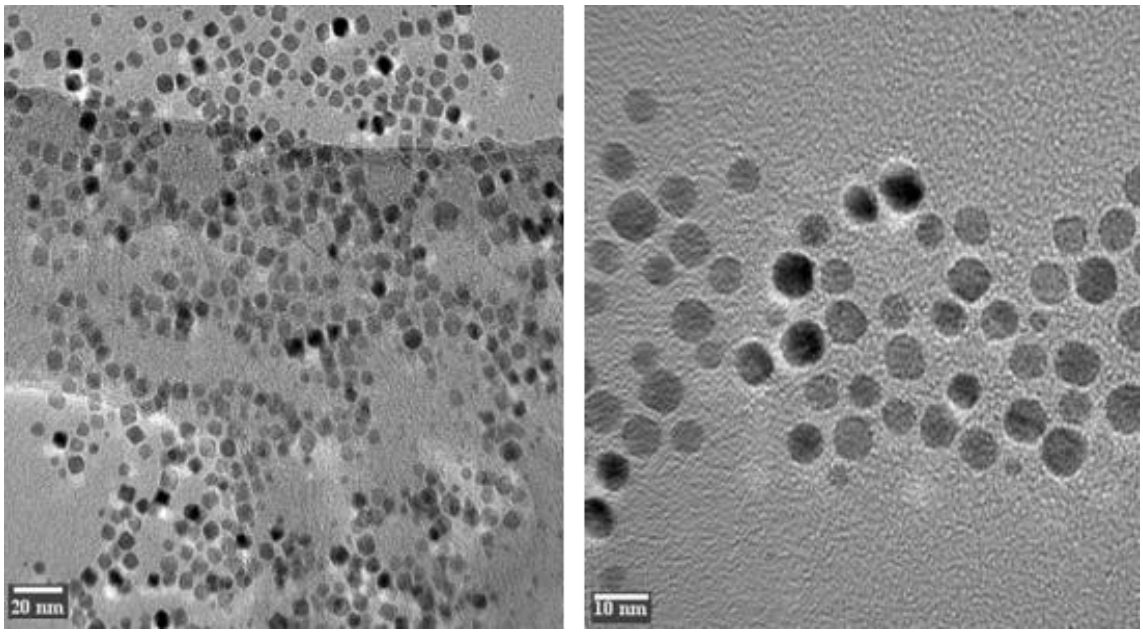

Figure 3.3: Pt NPs with truncated cuboctahedral morphology, which is the low surface energy Wulff shape for a face-centered cubic (FCC) metal.

3.2.4 Synthesis of Nanodendritic Clusters of Nanoparticles

In a typical synthesis, platinum metal salt was dissolved in an aqueous solution. By tuning the ratio of metal salt to surfactant (PVP), the diameter can be directed to smaller or increasingly large sizes. The metal salt solution and the surfactant containing solutions are allowed to equilibrate overnight separately. The solutions were mixed and sonicated for approximately half an hour prior to the reaction which evolves for 72 hours. The colorimetric change from pale yellow toward a dark

brown color indicates formation of platinum nanoparticles. Once the reaction is completed, the solution was centrifuged and washed via ethanol and hexane washing cycles before finally applying the nanoparticles to a TEM grid for characterization.

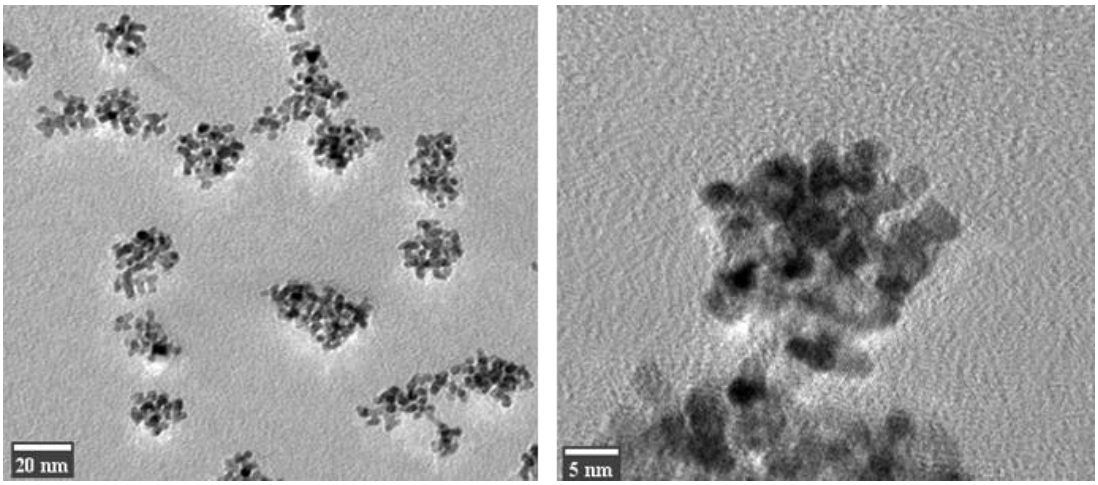

Figure 3.4: Nanoparticles with dendritic clustered morphology, the individual nanoparticles are ~2.5 nm and the clustered NPs are ~20 nm.

The weak reducing agent, L-ascorbic acid, is thought to not be able to readily reduce the Pt (IV) to Pt (0), however the particles undergo an autocatalytic process as opposed to a ripening process as the means of growth. The activity of nanodendrite structure is due to higher index facets occurring more readily than on a spherical shape where lower index facets dominate.

3.2.5 Synthesis of Polyhedral Seeds of Platinum

The Brust method for the generation of polyhedra is a rapid reduction of metal salt solution to zero valent colloid suspension. This is done by making a stock solution of metal acid solution in an acid buffer, this solution is allowed to equilibrate for a couple of days. A reducing solution of sodium borohydride (aqueous) is created and then quickly injected into the metal acid solution which should instantaneously become darker. The particles can be phase transferred from an aqueous medium to an organic solvent such as toluene by applying dodecanethiol to the particles.

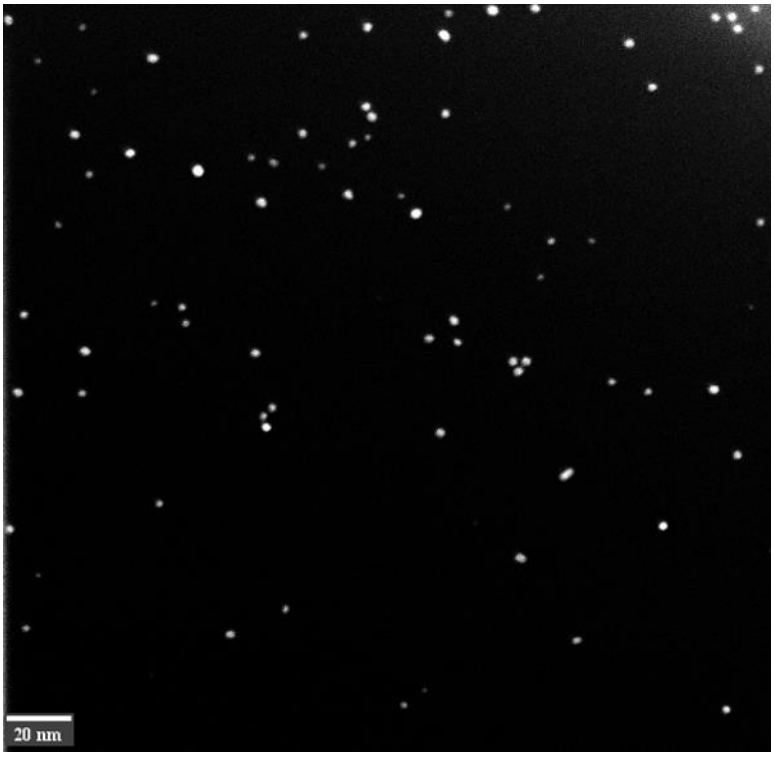

Figure 3.5: An angular dark field image of platinum nanopolyhedra with size of 2.61 ± 0.48nm.

Monodisperse anisotropic platinum nanoparticles were synthesized by polyol reduction with inverse micelles created by polyvinylpyrrolidone. The binding of Bromide ions to the (100) facets allowed for growth of the nanocubes to take place as the (111) facets were blocked.

Pt seeds of approximately 2.6 nm were created during the nucleation stage. These nuclei seeds are then grown by subsequent reduction of Pt ions onto the seeds. Should the reaction kinetics prove fast (higher temperature) the nanocrystals will tend toward a nanocube shape. This behavior is due to the bromide ions stabilizing the (100) faces. The Pt^{2+} ions are more easily reduced than the Pt^{4+} ions, thus the Pt^{2+} are reduced to form the nuclei while the Pt^{4+} ions attach to these nuclei seeds according to the reaction kinetics. The TEM image shows well-dispersed nanocrystals, with a degree of monodispersity of size as seen in Figure 3.6.

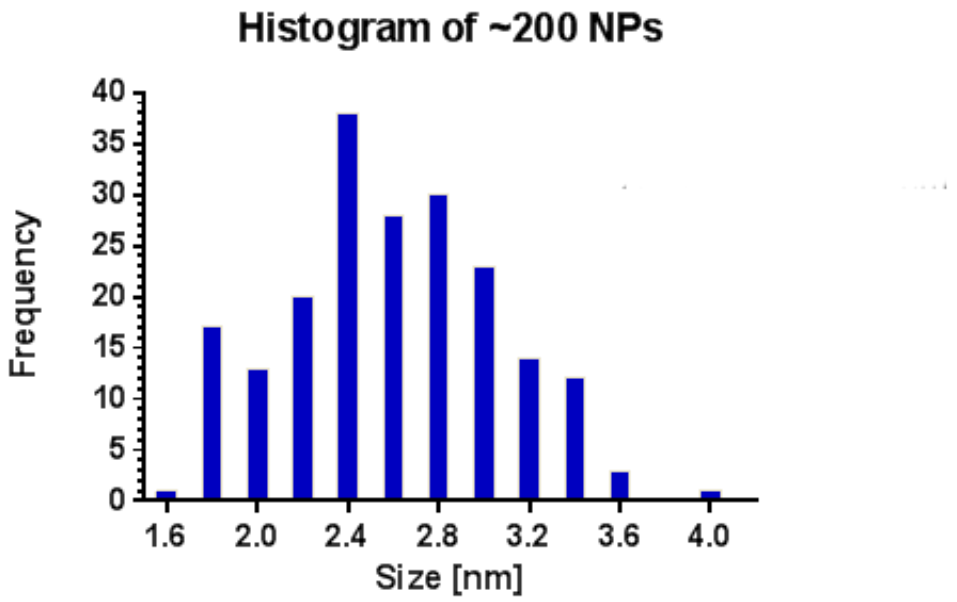

Figure 3.6: Histogram of Pt nanopolyhedra from Figure 3.5, average size is ca. 2.61 ± 0.48nm.

The crystallinity of the nanopolyhedra was determined by using the JEOL 2100F HRTEM for bright field (BF) images. The crystallinity of a particle is determined by measuring the d-spacing of the particle in the HRTEM BF image. Utilizing a standard electron microscopy software package such Gatan Digital Micrograph or ImageJ, an area of interest is selected by created a box around the nanoparticle and then the Fast Fourier Transform (FFT) command is applied. The generation of an FFT pattern is shown in the inset image of Figure 3.7. ImageJ was also used to clarify scale bars in Pt NPs images by re-creation of mapping of known scale bar to pixels of images. By measuring the distances from point to point in the FFT, a reasonably good approximation of the d-spacing can be found for specific crystalline planes (hkl), as seen in Table 1.

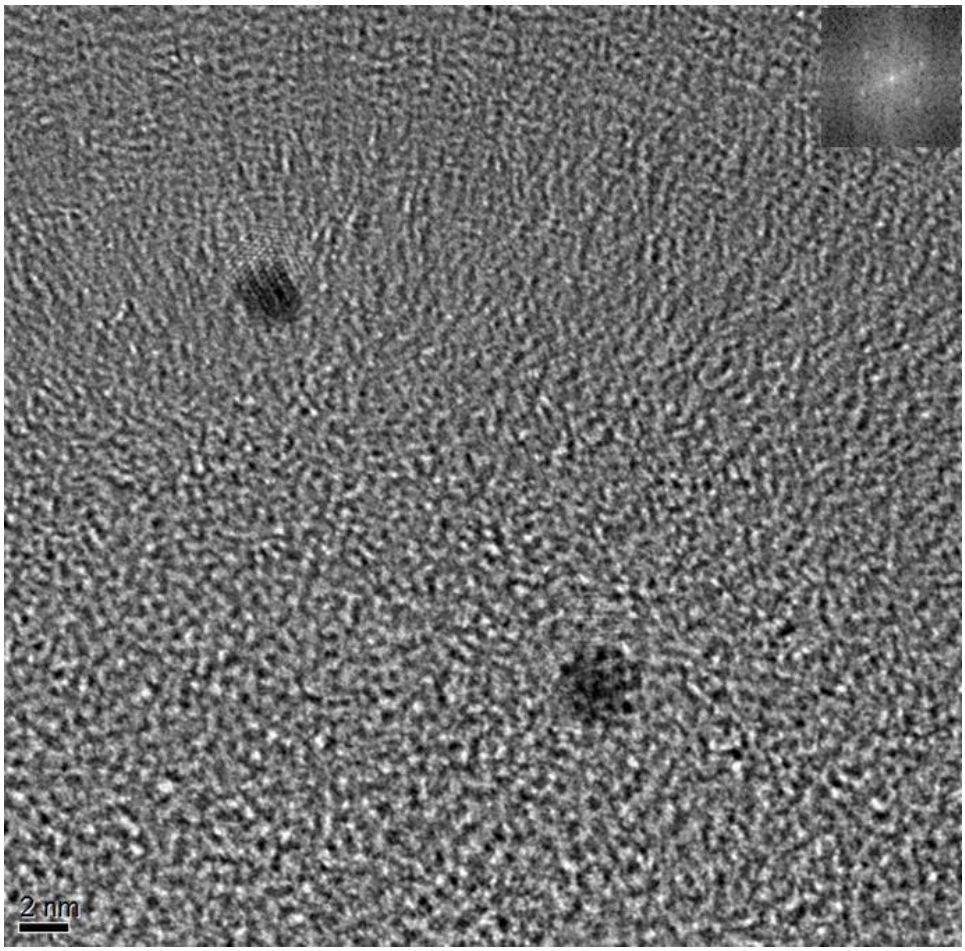

Figure 3.7: Bright-field image of nanoparticles with d-spacing measurements for specific (hkl) planes with inset FFT pattern.

Table 1: Verification of Crystalline Platinum Nanoparticles by FFT

Pt	d [A]	h	k	l	FFT [nm-1]	Measured [nm]
	2.265	1	1	1	8.88	0.225225
	1.9616	2	0	0	10.2	0.196078

The measured values correspond well with the platinum XRD data from the JCPDS database reference values. The values measured are at 0.563% error for the (111) facet and 0.041% error for the (200) facet. These crystalline platinum nanoparticles are ~2.6 nm in diameter.

3.3 CONCLUSIONS

Synthesis of Pt NPs of anisotropic shape was accomplished by using polyol reduction of metal precursors in the presence of surfactants and shape-directing species. The use of PVP micelles constrained the particles to yield nanoparticles < 6nm. The addition of a surfactant species to the reaction mixture serves a dual purpose, that of a size and shape mediator, as well as forming a protective layer around the nanocrystal which hinders agglomeration of the nanoparticles. The effect of de-agglomeration comes from the repulsion mechanism of the surfactant toward one-another. In the case of micellar encapsulation, the micelles hold the nanoparticle within the hydrophilic core in this water-in-oil system, while the hydrophobic tails repel each other, keeping the particle separated.

The amount of initial nanoparticle seeds is heavily influenced by the kinetics of the reaction setup, whereby a large number of smaller nanocrystals will nucleate or a smaller number of larger nanocrystals will form from the reaction medium into the suspension. In the case of the clustered nanocrystals, the reduction is purposely slowed so that the process of autocatalytic reduction can occur. The nucleation of a particle onto another particle allows the reduction to proceed. This process can only happen in the presence of a weak reducing agent, where the reduction rate is slow and in the absence of surfactants as they would hinder the process of autocatalytic reduction.

The addition of Halide ions such as Br^- ions in particular, strongly bind onto (100) facets. The concentration of halide ions around (100) facets is significantly higher than that around the other facets. Citrate ions are able to competitively adhere to the surface of the nanocrystal, which can be used to retard or hinder the oxidative etching process[48]. Based on the success of Br- ions to bind the (100) facets, we investigated the growth of Pt nanoparticles into anisotropic shapes. Facet-specific capping agents allowed for tighter monodispersity of size and morphology by limiting growth rates of selected facets. The Br- ions were effective in creating monodisperse nanoparticles under 6 nm, while the Cl- ions had less impact in the overall anisotropic morphology of the Pt nanoparticles. The TEM and STEM dark field allowed for determination of size distribution as well as morphological determination.

4.0 CARBON-ENCAPSULATED IRON NANOPARTICLES

4.1 INTRODUCTION

Carbon-encapsulated Fe (Fe@C) NPs have been shown to be useful as precursors to carbide heterostructures, such as SiC nanocones and Y- and T- heterostructures. Liu et al. speculated that these unusual nanostructures are due to the escape and agglomeration of the Fe from the C during the catalyzed formation of SiC[7,8]. In situ study of Fe@C NPs allowed us to see the dynamics of reaction environment on the environmental stability of the encapsulated metal nanoparticle as well as gain key insights once these nanostructures start to break down.

The viability of these core-shell NPs for industrial applications such as catalysis depends on the material's structural stability under operating conditions. The structural stability of a catalyst is an important factor to investigate during normal operations as using these catalysts involve high temperature processes[21], yet they are unstable at temperatures far below the melting temperature in the bulk[22].

Here we report the preparation of carbon-encapsulated iron (Fe@C) nanoparticles (NPs) catalysts and their thermal (in)stability characterization via in situ transmission electron microscopy, scanning electron microscopy, and scanning transmission electron microscopy (TEM, SEM, STEM). Fe@C NPs are synthesized via chemical vapor deposition (CVD) of ferrocene and toluene at elevated temperature (~1000 °C). Environmental transmission electron microscopy (ETEM) and SEM/STEM study in situ migration and release of Fe encapsulated in graphitic shells was performed. HRTEM allows for size and morphological analysis of the Fe NPs as well as inspection of the graphitic shell layers. Analysis of surface morphology and migration of particles

was performed to show that both Ostwald ripening and agglomeration of the Fe nanoparticles occurs at elevated temperatures. The ripening and coalescence of carbon encapsulated iron nanoparticles occurred once the iron left their shells and the mechanism of coarsening is dependent of the size of the iron NP crystallite.

4.2 EXPERIMENTAL

The experiments were carried out in a horizontal tube furnace via a floating catalytic chemical vapor deposition (CVD). Carbon-encapsulated Fe NPs were synthesized via the catalytic pyrolysis of toluene in the presence of ferrocene at 800-1000 °C. Toluene acts as the carbon source with ferrocene acting as the iron source, with an average iron core size of ~12nm and approximately 75nm for the entire core-shell encapsulated structure. As the sublimation temperature for ferrocene is quite low at ~100 °C, then within the low temperature region (120-140 °C), the ferrocene can evaporate and be carried toward the higher temperature zone of the tube furnace. There it thermally decomposes and is subsequently reduced into iron atom clusters, which can act as catalysts for the pyrolysis of the hydrocarbon that form carbon-encapsulated iron nanoparticles. Adjusting the parameters of both the carbon and metal source initially supplied, carbon-encapsulated structures with different core metal sizes and carbon shell thicknesses can be obtained.

An argon flow of 150 ml min^{-1} bubbles through toluene into the quartz tube chamber while a separate flow of Ar acts as the carrier gas. The flow of carrier gas can be modified to

allow more or less particle formation in the 500-1000 ml min^{-1} range. The schematic representation of the reaction and the resultant products are shown in Figure 4.1.

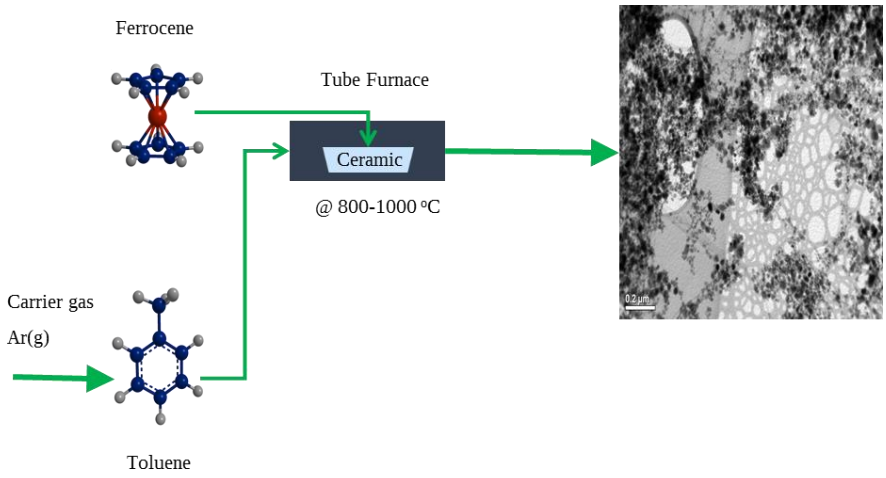

Figure 4.1: Schematic of the Catalytic Pyrolysis of Toluene and Ferrocene in a furnace and Fe@C NPs.

The resultant product was dispersed in ethanol by sonication; the nanoparticle suspension was added drop-wise to a Si/Si_3N_4 window (thickness of 50-100nm) and allowed to air dry. Dynamic observation of the metallic core nanocrystals was observed via in situ TEM.

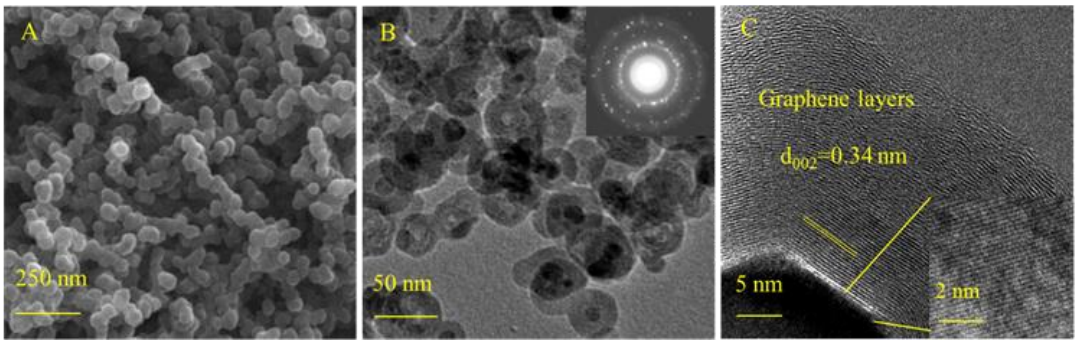

Figure 4.2: a) Scanning electron micrograph (SEM) image, b) transmission electron micrograph image, c) High resolution transmission electron micrograph (HRTEM) image of Fe@C NPs[70].

By utilizing in situ SEM/STEM at RJ Lee Group, Inc.[70], ripening and agglomeration processes of nanoparticle catalyst materials at industrially relevant conditions were visualized directly. We observed and analyzed the nanoparticle sintering and agglomeration behavior of the iron nanoparticles as they escaped the carbon shell.

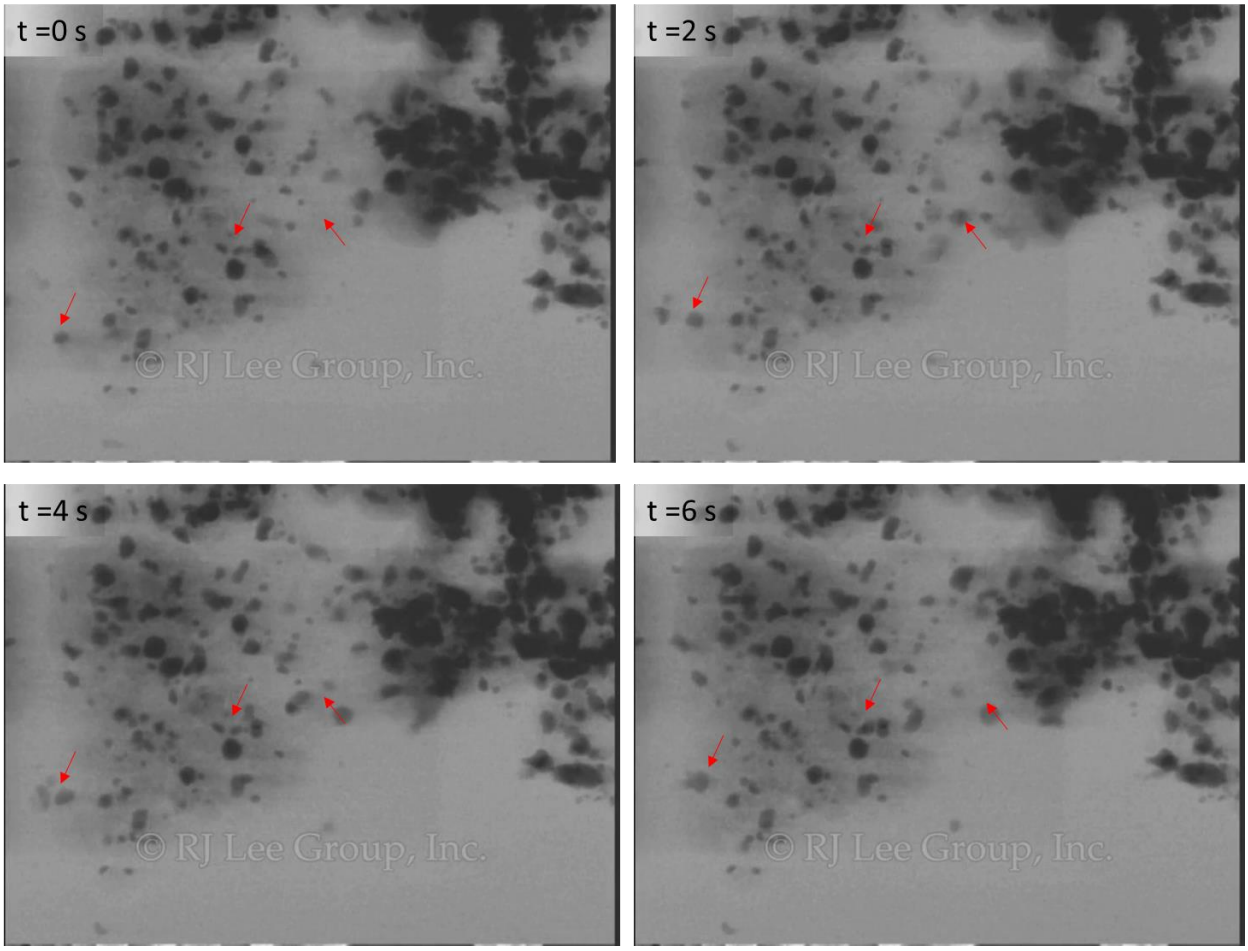

Figure 4.3: Snapshots of Fe NPs adhering and aggregrating outside their carbon shells with red arrows indicating areas of interest verification of iron nanoparticles moving on the outside of shells is verified by Figure 4.4.

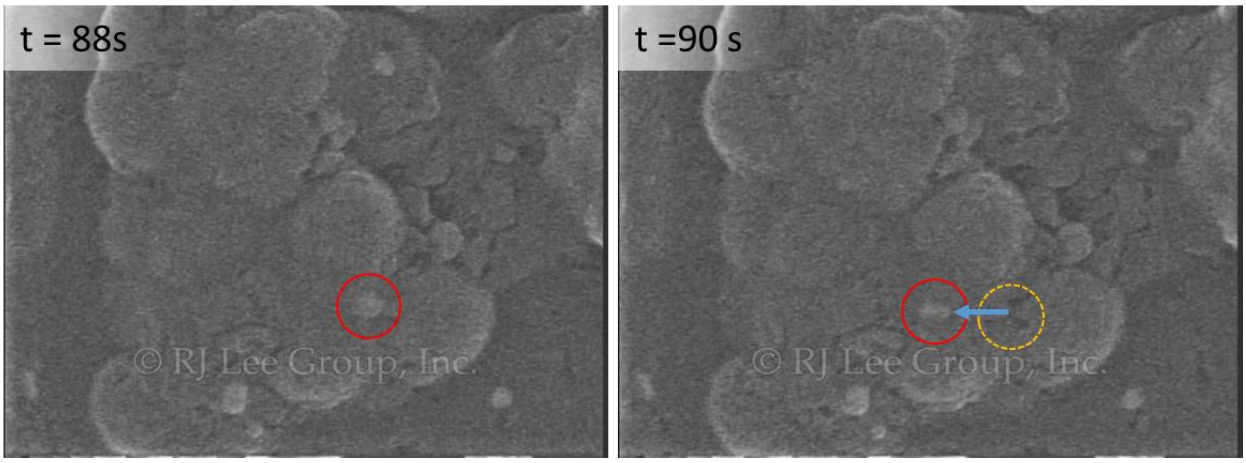

Figure 4.4: SEM/STEM images taken concurrently with images from Figure 4.3.

Many of the carbon shells appear to have lost their iron nanoparticle cores, due to particle migration and subsequent ripening of other larger particles. There seems to be fusion of larger particles, the smaller particles tend to shrink and vanish in a process of Ostwald ripening. The particle appears to undergo both processes, first losing mass to Ostwald effects and followed by particle migration on the surface as seen in Figure 4.3 and Figure 4.4, respectively. This effect seems to be mostly mediated by particle size and temperature effects, however there has been evidence of pressure within the core-shell acting as an impetus for particle migration through the protective graphitic shell[71].

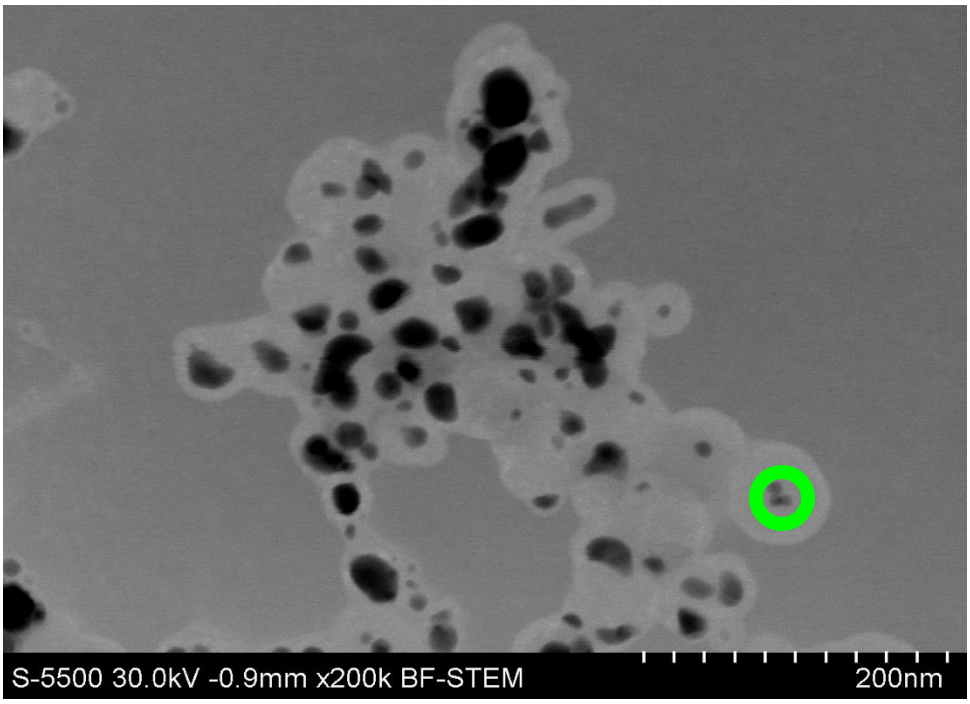

Figure 4.5: The above micrograph was taken from an *in situ* video that shows rapid movement 'liquid' movement of the Fe NPs. An Oswald ripening of particles and shrinking of other particles is implied.

4.3 RESULTS AND DISCUSSION

The 'liquid-like' behavior of the iron nanoparticles, as shown in Figure 4.5 indicates that the nanoparticles are escaping their carbon confinement and diffusing through the shell. Buffat et al. demonstrated that the temperature of solid-liquid transformation gold nanoparticles sharply decreases exponentially as the diameter of nanoparticles decreases[72]. The Fe NPs are able to coarsen via particle migration and Ostwald ripening mechanisms for larger particles and smaller particles, respectively. A particle of interest from Figure 4.5 is tracked in a time series of images which is compiled Figure 4.6.

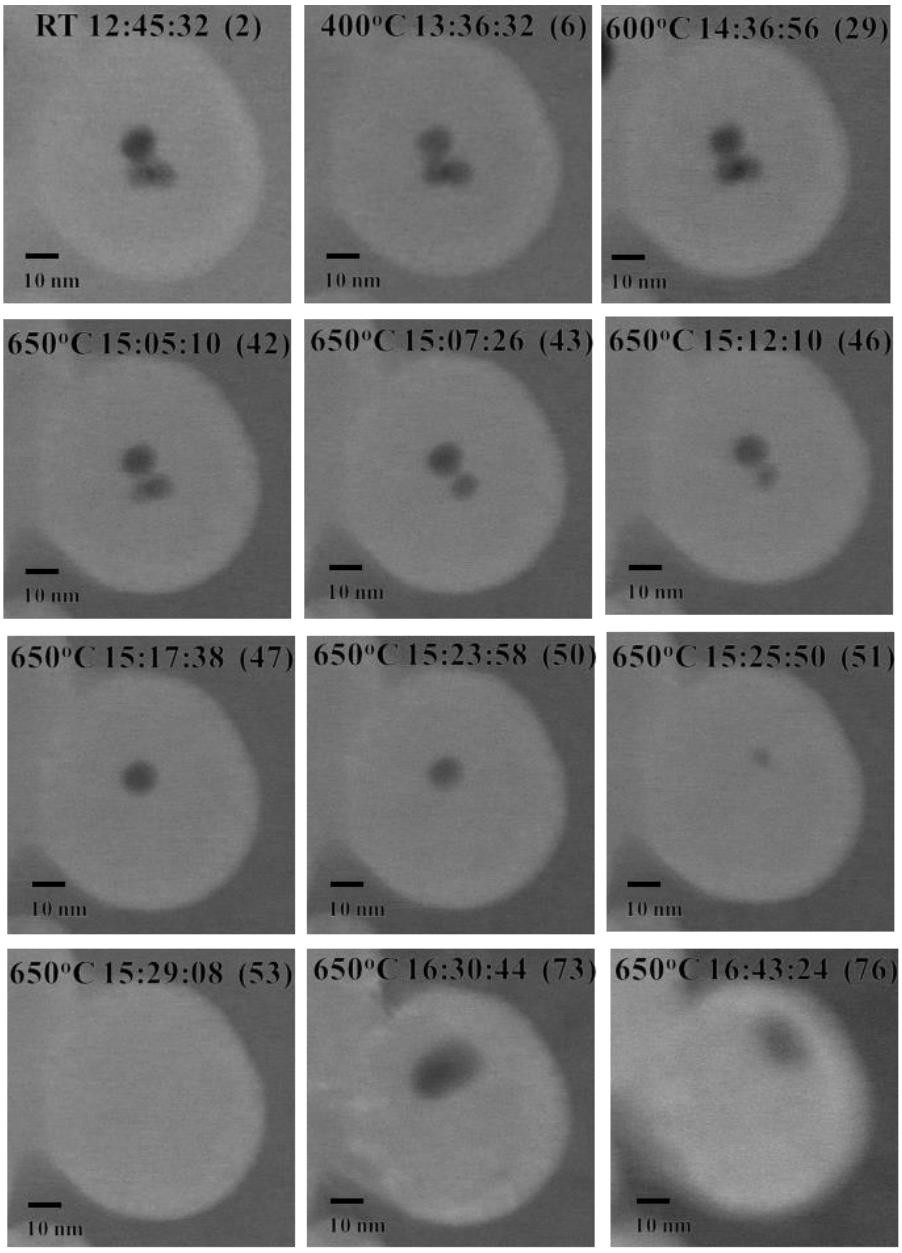

Figure 4.6: Fe nanoparticles losing mass via Oswald digestion of the Fe NP through carbon shell.

Figure 4.7 shows that smaller particles ~5nm undergo rapidly shrink on the order of minutes comparatively to hours in the previous case, Figure 4.6.

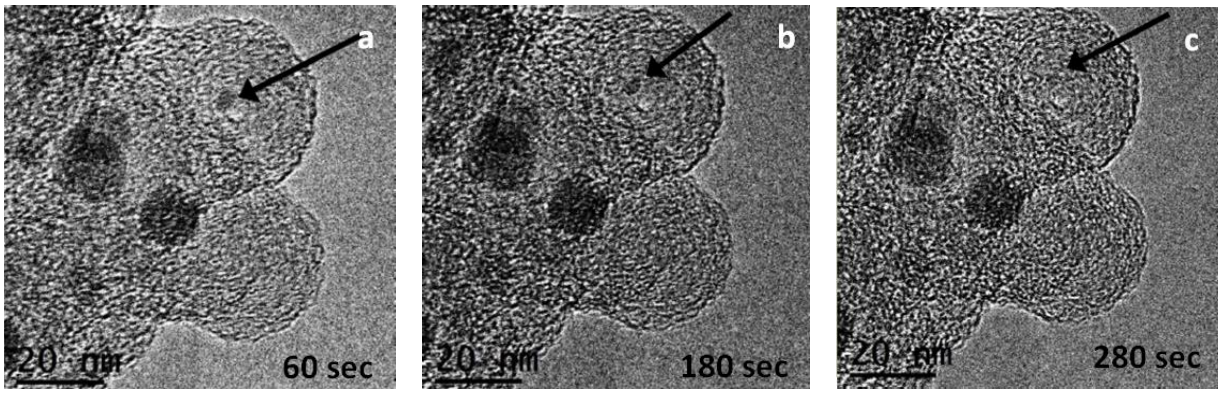

Figure 4.7: (a) Beginning of in situ observation at 700℃, 60 seconds after starting annealing. (b) After 180 seconds' annealing at 700℃. (c) After 280 seconds' annealing at 700℃.

The area of the particle is shrinking in accordance to an Ostwald digestion mechanism, wherein the radius particle of interest is shrinking over time and coarsening other nearby particles. The third to last frame (53) in Figure 4.6 shows that the area has been depleted. The last two time frames were included to show that the iron nanoparticles have completely left the shell are moving on the exterior of the carbonaceous shell.

In-situ observation of this phenomenon allows for a more intimate understanding of the role of particle size, environment, and support effects on the morphological restructuring of nanoparticle catalysts and their subsequent catalytic property. Electron beam damage and irradiation causes an immense pressure to be exerted upon the iron nanoparticle due to compressive force (GPa magnitude) which may account for the ability of metallic iron atoms to escape through the graphitic shells[71].

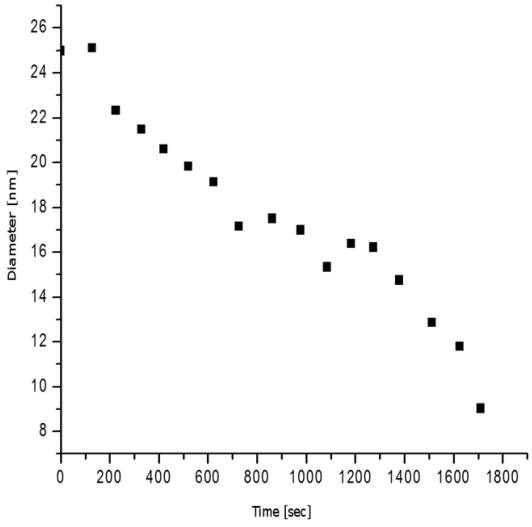

Figure 4.8: Fe nanoparticle showing Oswald digestion of tracked area in Figure 4.6.

The rate at which the particles degrade and subsequently ripen seems to be highly dependent on the radius or size of the particle. It was observed that larger particles tend to undergo particle coalescence and the smaller nanoparticles undergo the process of Ostwald digestion and ripening. The Ostwald digestion was observed to occur for particles under a threshold diameter of ~25nm as seen in Figure 4.8.

4.4 CONCLUSIONS

Iron encapsulated NPs were synthesized via pyrolysis of toluene and ferrocene. The migration of Fe NPs was observed via *in* situ TEM during elevated heating at ~650 C for several minutes to hours. The release of Fe NPs from their carbonaceous shell was attributed to elevated temperature

and electron beam induced compression of the carbon shell creating a driving force for the iron nanoparticles to release through the carbonaceous shell material. The agglomeration of nanoparticles only occurs once the Fe for the core escapes the shell and ripens on the exterior surface of the shell or the TEM grid support (SiN and carbon black).

5.0 CONCLUSIONS

In this thesis, I have studied the colloidal synthesis of anisotropic platinum nanoparticles and analyzed encapsulated iron nanoparticles. The Pt nanoparticles were synthesized with a seeded-mediated growth mechanism. Polyhedral seeds with a size range of 2.61 ± 0.48 nm were ripened into various anisotropic shapes, including nanocubes (5.1±2.3 nm), cuboctahedral (~8 nm), truncated cuboctahedral (~8), and nanoflower clusters (individual particles are ~2.5 nm, while the clusters are in the range of 20-30 nm), through a combination of selecting temperature and reducing conditions as well as the method of dispersion control through choice of surfactant.

Facet-specific capping agents allowed for tighter monodispersity of size and morphology by limiting growth rates of selected facets. The Br- ions were effective in creating monodisperse nanoparticles under 6 nm, while the Cl- ions had less impact in the overall anisotropic morphology of the Pt nanoparticles. The Br- ions adhere to the (100) facets and only allow growth of the on the other lower index facets (111) and (110). This led to anisotropic Pt morphologies to be grown, which coupled with PVP yielded monodisperse nanoparticle size and shapes. The concentration of Br- ion gave rise to different morphologies by changing the reduction/growth direction of the nanocrystals.

The reduction species and concentration is directly correlated to the rate of growth. A rapid reduction yields a higher amount of smaller particles, while a slower initial reduction yields a relatively less amount of larger nanoparticles. In the case of two-step reactions, the first step can be fast to yield numerous small seeds and in the secondary growth step can a slow reduction to allow particles to coarsen into the prescribed morphology desired. In the case of the clustered nanocrystal flowers, the reduction is purposely slowed so that the process of autocatalytic

reduction can occur. The nucleation of a particle onto another particle allows the reduction to proceed. This process can only happen in the presence of a weak reducing agent, where the reduction rate is slow and in the absence of surfactants as they would hinder the process of autocatalytic reduction.

A higher temperature synthesis tends to yield a rapid nucleation step with a minimized growth step and these nanocrystals tend toward lower surface energy morphologies that approximate polyhedral morphology. A lower temperature synthesis is not only energetically cheaper but allows for growth of nanoparticles with a higher degree anisotropy. Nanocubes needed a lower temperature to stabilize the colloid and allow growth, and spherical polyhedral shapes needed higher temperature for synthesis to create more small seeds. These nanocrystals are less energetically stable, however they contain more interesting features such as differing facets from their base Wulff shape.

For the iron encapsulated NPs, these synthesized via pyrolysis of toluene and ferrocene. In-situ observation of carbon encapsulated iron nanoparticles allows for a more intimate understanding of the role of particle size, environment, and support effects on the morphological restructuring of nanoparticle catalysts and their subsequent catalytic property. Carbon encapsulated Fe nanoparticles were to be used as catalyst materials for the growth of SiC Y & T shaped nanocone shaped wires. Electron beam damage and irradiation causes an immense pressure to be exerted upon the iron nanoparticle due to compressive force (GPa magnitude) which may account for the ability of metallic iron atoms to escape through the graphitic shells[71]. The rate at which the particles degrade and subsequently ripen seems to be highly dependent on the radius or size of the particle. The agglomeration of nanoparticles only occurs once the Fe from the core

escapes the shell and ripens on the exterior surface of the shell or the TEM grid support (SiN and carbon black).

It was observed via *in* situ TEM during elevated heating at ~650 C for several minutes to hours that larger particles tend to under particle coalescence and the smaller nanoparticles undergo the process of Ostwald digestion and ripening. The Ostwald digestion was observed to occur for particles under a threshold diameter of ~25nm. Nanoparticles at a diameter of ~40nm and above tend to undergo the process of particle coalescence.

Research into in-situ electron microscopy systems has massive potential to allow for understanding of precise mechanisms nucleation and growth dynamically. Recent work by Haimei Zheng et al. showed in-situ growth of anisotropic nanocrystals[75]. The ability to visualize the migration and growth of nanoparticles may yield enhanced insights into the growth, sintering, and inactivity/poisoning mechanisms of nanocatalyst particles. Recent work by Jorge Polte et al. has postulated and experimentally validated via SAXS that overall colloidal stability rather than thermodynamic stability determines the minimal particle size of a synthetic system of colloidal nanoparticles[76,77].

The synthesis of more monodisperse iron nanoparticles, which are subsequently carburized with a more uniform shell thickness would be of interest to better test the conditions by which core-shell particles are protected from poisoning and how they can escape their shells. Recent work by Effenberger et al. has produced an economically attractive route for the preparation of magnetic nanoparticles by decomposition of Fe_3(acac) in the presence of 1,2-octanediol and cyclohexanol[78].

BIBLIOGRAPHY

1. Miyaura, N. & Suzuki, A. Palladium-Catalyzed Cross-Coupling Reactions of Organoboron Compounds. *Chem. Rev.* **95,** 2457–2483 (1995).
2. Narayanan, R. Recent advances in noble metal nanocatalysts for suzuki and heck cross-coupling reactions. *Molecules* **15,** 2124–2138 (2010).
3. Burda, C., Chen, X., Narayanan, R. & El-Sayed, M. a. Chemistry and Properties of Nanocrystals of Different Shapes. *Chem. Rev.* **105,** 1025–1102 (2005).
4. Martin, R. & Buchwald, S. L. Palladium-catalyzed suzuki-miyaura cross-coupling reactions employing dialkylbiaryl phosphine ligands. *Acc. Chem. Res.* **41,** 1461–1473 (2008).
5. Bravo-Suárez, J. J., Chaudhari, R. V. & Subramaniam, B. in 3–68 (2013). doi:10.1021/bk-2013-1132.ch001
6. in *Kinetics of Heterogeneous Catalytic Reactions* (eds. Boudart, M. & Djega-Mariadassou, G.) 155–193 (Princeton University Press, 1984).
7. Liu, Z., C. Yang, J., Srot, V., A. van Aken, P. & Rühle, M. *Formation of Silicon Carbide Y Junctions by the Coalescence of Catalysts*. (2009).
8. Liu, Z. *et al.* Crystalline silicon carbide nanocones and heterostructures induced by released iron nanoparticles. *Appl. Phys. Lett.* **93,** 233113 (2008).
9. Alex, S. & Tiwari, A. Functionalized Gold Nanoparticles: Synthesis, Properties and Applications—A Review. *J. Nanosci. Nanotechnol.* **15,** 1869–1894 (2015).
10. An, K. & Somorjai, G. A. Nanocatalysis I: Synthesis of Metal and Bimetallic Nanoparticles and Porous Oxides and Their Catalytic Reaction Studies. *Catal. Letters* **145,** 233–248 (2015).
11. Sneed, B. T., Young, A. P. & Tsung, C.-K. Building up strain in colloidal metal nanoparticle catalysts. *Nanoscale* **7,** 12248–12265 (2015).
12. LaMer, V. K. Nucleation in Phase Transitions. *Ind. Eng. Chem.* **44,** 1270–1277 (1952).
13. Tsung, C.-K. *et al.* Sub-10 nm Platinum Nanocrystals with Size and Shape Control: Catalytic Study for Ethylene and Pyrrole Hydrogenation. *J. Am. Chem. Soc.* **131,** 5816–5822 (2009).
14. Faraday, M. The Bakerian Lecture: Experimental Relations of Gold (and Other Metals) to Light. *Philos. Trans. R. Soc. London* **147,** 145–181 (1857).
15. Hirai, H., Nakao, Y. & Toshima, N. Preparation of Colloidal Transition Metals in Polymers by Reduction with Alcohols or Ethers. *J. Macromol. Sci. Part A - Chem.* **13,** 727–750 (1979).

16. Roldan Cuenya, B. *et al.* Solving the structure of size-selected Pt nanocatalysts synthesized by inverse micelle encapsulation. *J. Am. Chem. Soc.* **132,** 8747–8756 (2010).

17. Pileni, M.-P. The role of soft colloidal templates in controlling the size and shape of inorganic nanocrystals. *Nat. Mater.* **2,** 145–150 (2003).

18. Matos, J. *et al.* In situ coarsening study of inverse micelle-prepared Pt nanoparticles supported on γ-Al2O3: pretreatment and environmental effects. *Phys. Chem. Chem. Phys.* **14,** 11457 (2012).

19. Mostafa, S. *et al.* Shape-dependent catalytic properties of Pt nanoparticles. *J. Am. Chem. Soc.* **132,** 15714–15719 (2010).

20. Narayanan, R. & El-Sayed, M. a. Catalysis with transition metal nanoparticles in colloidal solution: Nanoparticle shape dependence and stability. *J. Phys. Chem. B* **109,** 12663–12676 (2005).

21. Song, Y. *et al.* Controlled Synthesis of 2-D and 3-D Dendritic Platinum Nanostructures. *J. Am. Chem. Soc.* **126,** 635–645 (2004).

22. Luwang, M. N. *et al.* Surface chemistry of surfactant AOT-stabilized SnO(2) nanoparticles and effect of temperature. *J. Colloid Interface Sci.* **349,** 27–33 (2010).

23. Salzemann, C. & Petit, C. Influence of hydrogen on the morphology of platinum and palladium nanocrystals. *Langmuir* **28,** 4835–4841 (2012).

24. Ferrando, R., Jellinek, J. & Johnston, R. L. Nanoalloys: From Theory to Applications of Alloy Clusters and Nanoparticles. *Chem. Rev.* **108,** 845–910 (2008).

25. Fan, X., McLeod, M. C., Enick, R. M. & Roberts, C. B. Preparation of silver nanoparticles via reduction of a highly CO2-soluble hydrocarbon-based metal precursor. *Ind. Eng. Chem. Res.* **45,** 3343–3347 (2006).

26. Reuter, S., Hofmann, A. M., Busse, K., Frey, H. & Kressler, J. Langmuir and Langmuir-Blodgett films of multifunctional, amphiphilic polyethers with cholesterol moieties. *Langmuir* **27,** 1978–89 (2011).

27. Li, W., Waje, M., Chen, Z., Larsen, P. & Yan, Y. Platinum nanopaticles supported on stacked-cup carbon nanofibers as electrocatalysts for proton exchange membrane fuel cell. *Carbon N. Y.* **48,** 995–1003 (2010).

28. Baker, L. R. *et al.* Furfuraldehyde Hydrogenation on Titanium Oxide-Supported Platinum Nanoparticles Studied by Sum Frequency Generation Vibrational Spectroscopy: Acid–Base Catalysis Explains the Molecular Origin of Strong Metal–Support Interactions. *J. Am. Chem. Soc.* **134,** 14208–14216 (2012).

29. Krier, J. M. *et al.* Sum Frequency Generation Vibrational Spectroscopy of Colloidal Platinum Nanoparticle Catalysts: Disordering versus Removal of Organic Capping. *J. Phys. Chem. C* **116,** 17540–17546 (2012).

30. Geukens, I. & De Vos, D. E. Organic Transformations on Metal Nanoparticles: Controlling Activity, Stability, and Recyclability by Support and Solvent Interactions. *Langmuir* **29,** 3170–3178 (2013).

31. Al-Johani, H. *et al.* The structure and binding mode of citrate in the stabilization of gold nanoparticles. *Nat. Chem.* **9,** 890 (2017).

32. Scheeren, C. W., Machado, G., Dupont, J., Fichtner, P. F. P. & Texeira, S. R. Nanoscale Pt(0) particles prepared in imidazolium room temperature ionic liquids: synthesis from an organometallic precursor, characterization, and catalytic properties in hydrogenation reactions. *Inorg. Chem.* **42,** 4738–42 (2003).

33. Liu, He, F., Durham, E., Zhao, D. & Roberts, C. B. Polysugar-Stabilized Pd Nanoparticles Exhibiting High Catalytic Activities for Hydrodechlorination of Environmentally Deleterious Trichloroethylene. *Langmuir* **24,** 328–336 (2008).

34. Joo, S. H. *et al.* Thermally stable Pt/mesoporous silica core-shell nanocatalysts for high-temperature reactions. *Nat. Mater.* **8,** 126–131 (2009).

35. Im, S. H., Lee, Y. T., Wiley, B. & Xia, Y. Large-Scale Synthesis of Silver Nanocubes: The Role of HCl in Promoting Cube Perfection and Monodispersity. *Angew. Chemie Int. Ed.* **44,** 2154–2157 (2005).

36. Aiken, J. D. & Finke, R. G. A review of modern transition-metal nanoclusters: their synthesis, characterization, and applications in catalysis. *J. Mol. Catal. A Chem.* **145,** 1–44 (1999).

37. Verwey, E. J. . & Overbeek, J. T. . Theory of the stability of lyophobic colloids. *J. Colloid Sci.* **10,** 224–225 (1955).

38. Xia, Y., Xiong, Y., Lim, B. & Skrabalak, S. E. Shape-Controlled Synthesis of Metal Nanocrystals: Simple Chemistry Meets Complex Physics? *Angew. Chemie Int. Ed.* **48,** 60–103 (2009).

39. Habas, S. E., Lee, H., Radmilovic, V., Somorjai, G. A. & Yang, P. Shaping binary metal nanocrystals through epitaxial seeded growth. *Nat. Mater.* **6,** 692–7 (2007).

40. Wu, J. & Yang, H. Synthesis and electrocatalytic oxygen reduction properties of truncated octahedral Pt3Ni nanoparticles. *Nano Res.* **4,** 72–82 (2011).

41. Wang, C., Daimon, H., Lee, Y., Kim, J. & Sun, S. Synthesis of Monodisperse Pt Nanocubes and Their Enhanced Catalysis for Oxygen Reduction. *J. Am. Chem. Soc.* **129,** 6974–6975 (2007).

42. Wu, Y., Cai, S., Wang, D., He, W. & Li, Y. Syntheses of water-soluble octahedral, truncated octahedral, and cubic Pt-Ni nanocrystals and their structure-activity study in model hydrogenation reactions. *J. Am. Chem. Soc.* **134,** 8975–8981 (2012).

43. Lee, H., Habas, S. E., Somorjai, G. a. & Yang, P. Localized Pd overgrowth on cubic Pt nanocrystals for enhanced electrocatalytic oxidation of formic acid. *J. Am. Chem. Soc.* **130,** 5406–5407 (2008).

44. Zhang, J., Yang, H., Fang, J. & Zou, S. Synthesis and Oxygen Reduction Activity of Shape-Controlled Pt_3Ni Nanopolyhedra. *Nano Lett.* **10,** 638–644 (2010).

45. Wu, J., Gross, A. & Yang, H. Shape and composition-controlled platinum alloy nanocrystals using carbon monoxide as reducing agent. *Nano Lett.* **11,** 798–802 (2011).

46. Carpenter, M. K., Moylan, T. E., Kukreja, R. S., Atwan, M. H. & Tessema, M. M. Solvothermal synthesis of platinum alloy nanoparticles for oxygen reduction electrocatalysis. *J. Am. Chem. Soc.* **134,** 8535–8542 (2012).

47. Zheng, Y., Zeng, J., Ruditskiy, A., Liu, M. & Xia, Y. Oxidative Etching and Its Role in Manipulating the Nucleation and Growth of Noble-Metal Nanocrystals. *Chem. Mater.* **26,** 22–33 (2014).

48. Xiong, Y., McLellan, J. M., Yin, Y. & Xia, Y. Synthesis of palladium icosahedra with twinned structure by blocking oxidative etching with citric acid or citrate ions. *Angew. Chemie - Int. Ed.* **46,** 790–794 (2007).

49. Jiang, H.-L., Akita, T. & Xu, Q. A one-pot protocol for synthesis of non-noble metal-based core–shell nanoparticles under ambient conditions: toward highly active and cost-effective catalysts for hydrolytic dehydrogenation of NH3BH3. *Chem. Commun.* **47,** 10999 (2011).

50. Sun, C. *et al.* Tumor-targeted drug delivery and MRI contrast enhancement by chlorotoxin-conjugated iron oxide nanoparticles. *Nanomedicine (Lond).* **3,** 495–505 (2008).

51. McBain, S. C., Yiu, H. H. P. & Dobson, J. Magnetic nanoparticles for gene and drug delivery. *Int. J. Nanomedicine* **3,** 169–180 (2008).

52. Fultz, B. & Howe, J. M. *Transmission Electron Microscopy and Diffractometry of Materials*. *Transmission Electron Microscopy and Diffractometry of Materials* (Springer Berlin Heidelberg, 2008). doi:10.1007/978-3-540-73886-2

53. Williams, D. B. & Carter, C. B. *Transmission electron microscopy: A textbook for materials science*. *Transmission Electron Microscopy: A Textbook for Materials Science* (Springer US, 2009). doi:10.1007/978-0-387-76501-3

54. in *Aberration-Corrected Imaging in Transmission Electron Microscopy* 15–51 (IMPERIAL COLLEGE PRESS, 2015). doi:10.1142/9781783265299_0002

55. Nenad M. Markovic, Gasteiger, H. a. & Ross, P. N. Oxygen Reduction on Platinum Low-Index Single-Crystal Surfaces in Sulfuric Acid Solution: Rotating Ring-Pt(hkZ) Disk Studies. *J. Phys. Chem.* **99,** 3411 (1995).

56. Chen, J., Xiong, Y., Yin, Y. & Xia, Y. Pt nanoparticles surfactant-directed assembled into colloidal spheres and used as substrates in forming Pt nanorods and nanowires. *Small* **2,** 1340–1343 (2006).

57. Tian, N., Zhou, Z.-Y., Sun, S.-G., Ding, Y. & Wang, Z. L. Synthesis of Tetrahexahedral Platinum Nanocrystals with High-Index Facets and High Electro-Oxidation Activity. *Science (80-.).* **316,** 732–735 (2007).

58. Sanchez, S. I., Small, M. W., Zuo, J. & Nuzzo, R. G. Structural Characterization of Pt - Pd and Pd - Pt Core Shell\nNanoclusters at Atomic Resolution. *J. Am. Chem. Soc.* **131,** 8683–8689 (2009).

59. Thomas, J. M. & Williams, R. J. P. Catalysis: principles, progress, prospects. *Philos. Trans. R. Soc. A Math. Phys. Eng. Sci.* **363,** 765–791 (2005).

60. Li, D. *et al.* Direction-Specific Interactions Control Crystal Growth by Oriented Attachment. *Science (80-.).* **336,** 1014–1018 (2012).

61. Park, Y. K., Tadd, E. H., Zubris, M. & Tannenbaum, R. Size-controlled synthesis of alumina nanoparticles from aluminum alkoxides. *Mater. Res. Bull.* **40,** 1506–1512 (2005).

62. Allard, L. F. *et al.* Evolution of gold structure during thermal treatment of Au/FeOx catalysts revealed by aberration-corrected electron microscopy. *J. Electron Microsc. (Tokyo).* **58,** 199–212 (2009).

63. Meena, S. K. *et al.* The role of halide ions in the anisotropic growth of gold nanoparticles: a microscopic, atomistic perspective. *Phys. Chem. Chem. Phys.* **18,** 13246–13254 (2016).

64. Meena, S. K. & Sulpizi, M. From Gold Nanoseeds to Nanorods: The Microscopic Origin of the Anisotropic Growth. *Angew. Chemie Int. Ed.* **55,** 11960–11964 (2016).

65. Meena, S. K. & Sulpizi, M. Understanding the Microscopic Origin of Gold Nanoparticle Anisotropic Growth from Molecular Dynamics Simulations. *Langmuir* **29,** 14954–14961 (2013).

66. Tsung, C.-K. *et al.* Sub-10 nm Platinum Nanocrystals with Size and Shape Control: Catalytic Study for Ethylene and Pyrrole Hydrogenation. *J. Am. Chem. Soc.* **131,** 5816–5822 (2009).

67. Bratlie, K. M., Lee, H., Komvopoulos, K., Yang, P. & Somorjai, G. a. Platinum nanoparticle shape effects on benzene hydrogenation selectivity. *Nano Lett.* **7,** 3097–3101 (2007).

68. Shao, M., Yu, T., Odell, J. H., Jin, M. & Xia, Y. Structural dependence of oxygen reduction reaction on palladium nanocrystals. *Chem. Comm.* **47,** 6566–8 (2011).

69. Lim, B. *et al.* Pd-Pt Bimetallic Nanodendrites with High Activity for Oxygen Reduction. *Science (80-.).* **324,** 1302–1305 (2009).

70. Sturgeon, J. L. *et al.* In Situ Heating, Imaging, and Analysis of Nanoparticles using SEM, STEM, and XPS. in *In Situ Microscopy/Spectroscopy - Interfacial Chemistry/Catalysis presented at the 57th AVS International Symposium & Exhibition* (2010).

71. Banhart, F. & Ajayan, P. M. Carbon onions as nanoscopic pressure cells for diamond formation. *Nature* **382,** 433–435 (1996).

72. Buffat, P. & Borel, J.-P. Size effect on the melting temperature of gold particles. *Phys. Rev. A* **13,** 2287–2298 (1976).

73. Illés, E. *et al.* Novel carboxylated PEG-coating on magnetite nanoparticles designed for biomedical applications. *J. Magn. Magn. Mater.* **380,** 132–139 (2015).

74. Kirillova, A. *et al.* Hybrid Hairy Janus Particles Decorated with Metallic Nanoparticles for Catalytic Applications. *ACS Appl. Mater. Interfaces* **7,** 21218–21225 (2015).

75. Liao, H.-G. *et al.* Facet development during platinum nanocube growth. *Science (80-.).* **345,** 916–919 (2014).

76. Wuithschick, M., Witte, S., Kettemann, F., Rademann, K. & Polte, J. Illustrating the formation of metal nanoparticles with a growth concept based on colloidal stability. *Phys. Chem. Chem. Phys.* **17,** 19895–19900 (2015).

77. Wuithschick, M. *et al.* Turkevich in New Robes: Key Questions Answered for the Most Common Gold Nanoparticle Synthesis. *ACS Nano* **9,** 7052–7071 (2015).

78. Rossi, F. B. E. and R. A. C. and P. K. K. and G. M. and S. H. M. and R. F. J. and L. M. Economically attractive route for the preparation of high quality magnetic nanoparticles by the thermal decomposition of iron(III) acetylacetonate. *Nanotechnology* **28,** 115603 (2017).